Body-of-revolution finite-difference time-domain modeling of space–time focusing by a three-dimensional lens

David B. Davidson

Department of Electrical and Electronic Engineering, University of Stellenbosch, Stellenbosch 7600, South Africa

Richard W. Ziolkowski

Electromagnetics Laboratory, Department of Electrical and Computer Engineering, University of Arizona, Tucson, Arizona 85721

We introduce a body-of-revolution finite-difference time-domain simulation capability that can be applied to rotationally symmetric linear-optics problems. This simulator allows us to reduce a computationally intractable, three-dimensional problem to a numerically solvable two-dimensional one. It is used to model the propagation of a pulsed Gaussian beam through a thin dielectric lens and the focusing of the resulting pulsed beam. Analytic results for such a lens-focused, pulsed Gaussian beam are also derived. It is shown that, for the same input energy, one can design ultrawide-bandwidth driving signals to achieve a significantly larger intensity enhancement than is possible with equivalent many-cycle, monochromatic signals. Several specially engineered (designer) pulses are introduced that illustrate how one can achieve these intensity enhancements. The simulation results confirm that intensity enhancements can be realized with properly designed ultrawide-bandwidth pulses.

1. INTRODUCTION

Pulses that are shorter than 10 fs in duration and that contain only 4 cycles can now be generated. If one considers a 1.0-mJ, 10-fs pulse focused to a 1.0-μm spot, the resulting intensity at the focus is approximately 3×10^{18} W/cm^2. This is just below the threshold of the domain (10^{19} to 10^{21} W/cm^2) in which many researchers believe new physical effects in laser–matter interaction will occur. These effects include nonlinear (multiphoton) Compton scattering and the generation of large amplitude waves to accelerate particles. If there were a means to achieve more-intense foci with current systems, this realm could be reached more quickly.

With the development of these short-pulse, very intense laser systems, issues pertaining to the focusing of the resulting pulsed beams through a lens become important. In particular, one needs to know how the various lens magnification and waist formulas, which are derived for monochromatic signals, are modified when ultrawide-bandwidth (UWB) pulses are used. Any enhancements or degradations in the performance of a focused laser beam will significantly affect the use of these systems for laser–matter-interaction studies or device applications.

Since the size of the structures is of the order of a wavelength and the time duration of the pulses is extremely short, standard scalar, parabolic approximation models may not be adequate to simulate the optical focusing physics. More-accurate calculations are feasible, and possible approaches include the finite-difference time-domain (FDTD) solution of Maxwell's equations. As has been shown recently with nonlinear-FDTD simulations of self-focusing in nonlinear materials,[1] the full-wave vector approach leads to a more thorough understanding of pulsed-beam propagation in complex environments.

The FDTD approach is used in this paper to simulate the focusing of ultrashort, pulsed beams with a thin dielectric lens. The numerical results are compared with approximate analytical models. Both approaches establish that the rise time of a pulse plays a crucial role in the focusing process. Intensity enhancements over the continuous-wave (cw) results in the UWB case are demonstrated.

The organization of this paper is as follows. In Section 2 the FDTD method is reviewed, and the problems associated with applying a full three-dimensional (3D) formulation to an optical device such as a lens are discussed. We show that at present a full 3D formulation is at the limit of the realistic capacities of modern computers, even powerful massively parallel processors. As a result a FDTD formulation that exploits the rotational symmetry frequently present in both the lenses and the beams is presented in Section 3. We use this body-of-revolution (BOR) FDTD formulation in our research to reduce the problem space effectively to two dimensions, but we emphasize that the solution is three dimensional (we factor out the rotational variation analytically), and the code solves for all six field components governed by the full-wave vector Maxwell's equations. In Section 4 an analytical approach is presented that predicts the lens magnification and the waist size for pulses with ultrabroadband frequency content. The results that are generated with the BOR-FDTD simulator and that model the interaction of pulsed Gaussian beams with thin dielectric lenses are presented in Section 5. Simulation results are given for both UWB pulses and multicycle pulses,

with the latter approximating monochromatic sources. These numerical results are then compared with the analytical predictions developed in Section 4. Finally some conclusions are drawn in Section 6.

2. FINITE-DIFFERENCE TIME-DOMAIN METHOD

The FDTD method is now widely used in computational electromagnetics and was first introduced by Yee[2] almost three decades ago. The method discretizes Maxwell's equations with a second-order central-differencing scheme, with the electric and the magnetic fields being interleaved in time and space on staggered grids. The electric- and the magnetic-field components are successively updated by repeated implementation of the finite-difference equivalents of the curl equations; this process is widely known as leapfrog time marching. The scheme is an explicit scheme; no matrix inversion is required. Yee's initial research was directed at electromagnetically small problems with closed boundaries, but great strides were made in the subsequent decades. These developments included absorbing boundary conditions (ABC's) to simulate open boundaries, incident waves of arbitrary time duration and spatial variation, and the availability of very fast and capable computers with very large memory capacities. By the end of the 1980's, the FDTD approach had been applied to a number of large and complex problems. Two recent references on the subject are Chew's textbook,[3] which presents a very readable introduction to the method, and Taflove's research monograph,[4] which provides an overview of more complex applications.

The basic FDTD equations for the Cartesian coordinate system may be found in a number of references, including Refs. 3–5, and are not presented here. Suffice it to say that the density of the numerical sampling determines the accuracy of the method and that it has been widely accepted that a minimum of 10 samples/wavelength are required for adequate representation of the field amplitude and the phase. This heuristic, widely used in the computational electromagnetic community, was established when problems spanned only a few wavelengths. Cangellaris and Lee have recently shown it to be valid only for electromagnetically small structures[6]; as the electromagnetic size of the structure increases, so does the required number of samples per wavelength. This rule of thumb is required for containment of the grid dispersion errors.

To model a volume of size L^3, a standard FDTD simulator requires $(L/\Delta L)^3$ sample points, and we note that ΔL may be weakly problem-size dependent.[6] The number of computations for each time step is $\mathcal{O}(L/\Delta L)^3$. The time marching is generally repeated for a time that is usually related to the dimensions of the box; thus the run time of a 3D FDTD code is generally $\mathcal{O}(L/\Delta L)^4$. The constant associated with this estimate is approximately 50. Hence the run time grows as the fourth power of the problem dimension, and, since the sampling density must increase for large problems, as was discussed in the previous paragraph, the true rate of growth is slightly faster than this. For rapid execution it is essential that the complete discretized space be held in core memory; the memory requirement grows as $\mathcal{O}(L/\Delta L)^3$.

These estimates can be specified for linear-optics problems. Typical optical devices that might be encountered in fiber-optic systems have dimensions of several micrometers on a side, and typical sources in the near infrared have wavelengths of the order of 1 μm. This translates into a requirement of approximately a 100-nm maximum sample spacing. This means that the problem size will involve many millions of sample points, and the numerical complexity can easily approach a trillion (10^{12}) floating-point operations.

We have developed a FDTD 3D code in FORTRAN 90 for the Connection Machine Model CM-2. The largest problem that we have run used approximately one third of a million sample points to discretize a volume of approximately $20,000\lambda^3$ at $\lambda/10$ sampling and two planes of symmetry to reduce the problem to $5000\lambda^3$. The problem was a Gaussian beam propagating in free space, similar to the case presented in Ref. 7, Sec. 5. Solving this problem took approximately one half-hour on a 8192 processor CM-2 (one eighth of a full CM-2). Typical average sustained processor speed overall was approximately 50 megaFlops per second (Mflops/s) (after some optimization), slightly less than 3% of the claimed peak throughput of the system; for the finite-differencing operations approximately 5% of the peak was achieved. It is interesting to compare this with previous research by Davidson, who used transputer arrays for boundary-element frequency-domain calculations, in which efficiencies of 70–80% were obtained[8,9]; however, efficiency as used in Refs. 8 and 9 is not the same measurement as percentage of claimed peak throughput given here for the CM-2; the transputer arrays ran at approximately 25% of their claimed peak throughput. The performance degradation in the case of the transputers was due to the peak rate's being based on the program and the data's being stored entirely on the fast on-chip 4-kbyte random access memory. This scheme is not possible with any finite-difference or finite-element scheme with a nontrivial grid size.

Whereas moderately satisfactory results were obtained in this $5000\lambda^3$ case, increasing the sample density by only 2 exceeds the capacity of the computer. Thus even simple convergence tests cannot be performed. Nonlinear materials frequently require much higher sampling densities.[1] Hence we conclude that, given the current state of available massively parallel processors, modeling a realistic optical device in three dimensions is on the borderline of practicality: this may well change once new massively parallel processors such as the recently released CM-5 become available for modeling research.

3. BODY-OF-REVOLUTION FINITE-DIFFERENCE TIME-DOMAIN METHOD

A. Basic Formulation

Rotational symmetry has been widely exploited in frequency-domain boundary and volume element methods, which are normally called the method of moments in computational electromagnetics. Although this connotation was used by Harrington[10] for solving integral

equations, the term is sufficiently general to cover almost all the discrete methods. The BOR formulation assumes that the structure has rotational symmetry and expands the azimuthal dependence of the fields as a Fourier series. Each azimuthal mode in the series is orthogonal. For general excitations a large number of modes may be required, which can decrease the computational attractiveness of the approach. For the problems considered in this paper, which represent a significant class of actual optical-device–beam interactions, only one mode is necessary. This makes the computational and the memory requirements of the BOR-FDTD code essentially two dimensional.

The following development is based on Merewether and Fisher's paper.[5] This is one of the earliest and most thorough treatments of the BOR-FDTD approach. Very few references that use this approach with applications to scattering problems are available in the literature; however, it has been used recently with much success by the beam-physics community to study guided waves in accelerator cells, e.g., the azimuthal mode simulator (AMOS) code developed by DeFord at the Lawrence Livermore National Laboratory. Since many of these sources may not be readily accessible to everyone, the BOR-FDTD formulation is given explicitly below and in Appendix A.

We assume that the axis of rotational symmetry is the z axis. We assume an incident plane wave with the propagation vector $\mathbf{k}$ pointed toward the origin in the x–z plane (this can always be arranged given rotational symmetry) with the electric-field vector

$$\mathbf{E}^{inc} = E\left(t - \frac{\hat{k} \cdot \mathbf{R}}{c}\right)(-\hat{y} \times \hat{k}). \quad (1)$$

For this geometry

$$\hat{k} = \sin(\theta)\hat{x} - \cos(\theta)\hat{z}, \quad (2)$$

$$\hat{k} = \sin(\theta)\cos(\phi)\hat{\rho} - \sin(\theta)\sin(\phi)\hat{\phi} - \cos(\theta)\hat{z}, \quad (3)$$

$$-\hat{y} \times \hat{k} = \cos(\theta)\cos(\phi)\hat{\rho} - \cos(\theta)\sin(\phi)\hat{\phi} + \sin(\theta)\hat{z}, \quad (4)$$

$$\mathbf{R} = \rho\hat{\rho} + z\hat{z}, \quad (5)$$

$$\hat{k} \cdot \mathbf{R} = \rho \, \sin(\theta)\cos(\phi) - z \, \cos(\theta). \quad (6)$$

Hence E_ρ^{inc}, E_z^{inc} are even functions of ϕ and can be expressed in a Fourier cosine series. A similar expansion of the incident magnetic fields shows that H_ϕ^{inc} is also even. (A similar result may be derived for an impressed current source of the form $\mathbf{J} = J_s\{t - [(\hat{k} \cdot \mathbf{R})/c]\hat{n}\}$; in this case J_ρ and J_z are even.) The total fields (the sum of the incident and the scattered fields) will preserve this angular dependence; hence these field components can be expanded in terms of a Fourier cosine series. The E_ρ expansion is

$$E_\rho(r,z,\phi,t) = E_{\rho 0}(r,z,t) + \sum_{k=1}^{\infty} E_{\rho k}(r,z,t)\cos(k\phi), \quad (7)$$

$$E_{\rho 0}(r,z,t) = \frac{1}{2\pi}\int_0^{2\pi} E_\rho(r,z,\phi,t)\mathrm{d}\phi, \quad (8)$$

$$E_{\rho k}(r,z,t) = \frac{1}{\pi}\int_0^{2\pi} E_\rho(r,z,\phi,t)\cos(k\phi)\mathrm{d}\phi. \quad (9)$$

Similarly, E_ϕ (and J_ϕ), H_ρ, and H_z are odd and can be expanded in a Fourier sine series. The E_ϕ expansion is

$$E_\phi(r,z,\phi,t) = E_{\phi 0}(r,z,t) + \sum_{k=1}^{\infty} E_{\phi k}(r,z,t)\sin(k\phi), \quad (10)$$

$$E_{\phi k}(r,z,t) = \frac{1}{\pi}\int_0^{2\pi} E_\phi(r,z,\phi,t)\sin(k\phi)\mathrm{d}\phi. \quad (11)$$

The BOR-FDTD formulation proceeds with the writing of Maxwell's equations for each mode; the partial derivative in ϕ is performed analytically, and the other partial derivatives are approximated with the conventional central-differencing approach of the Yee scheme. The FDTD equations in rectangular coordinates are widely available, and the formulas for the BOR case are tabulated in Merewether and Fisher's paper (Ref. 5, Fig. 10, p. 33). Unfortunately this reference contains some minor typographical errors. We thus rederive and tabulate for completeness the discretized equations and the boundary conditions in Appendix A.

For the problems considered in this paper, the incident wave is propagating along the z axis with the form

$$\mathbf{E}^{inc} = f(x,y)E[t - (z/c)]\hat{x}, \quad (12)$$

where $f(x,y)$ is some rotationally symmetric weighting function. Written in the cylindrical coordinate system, the incident field is

$$\mathbf{E}^{inc} = f(\rho)E[t - (z/c)][\cos(\phi)\hat{\rho} - \sin(\phi)\hat{\phi}]. \quad (13)$$

For this case only the fields associated with the $k = 1$ mode are nonzero. This reduces the problem to a two-dimensional one. (Were higher-order modes present, a separate BOR-FDTD problem would have to be solved for each mode.)

The time-step size cannot be made arbitrarily large since the time marching can then become unstable. The upper limit on the temporal-step size is the well-known Courant–Friedrichs–Levy stability criterion.[3] In addition to the reduction of the problem computationally to two dimensions, the BOR-FDTD scheme has a further advantage in that the appropriate stability criterion for low azimuthal-mode numbers is near the two-dimensional one (Ref. 5, p. 32), $\Delta t_{2D} \le \Delta/(v_{max}\sqrt{2})$, where v_{max} is the maximum wave speed in the simulation space. In particular, if m is the azimuthal-mode number, the BOR-FDTD stability criterion is

$$\Delta t \le \frac{1}{v_{max}}\left\{\frac{1}{\Delta\rho^2}\frac{[(m+1)^2 + 2.8]}{4} + \frac{1}{\Delta z^2}\right\}^{-1/2}. \quad (14)$$

If the spatial discretizations $\Delta\rho = \Delta z = \Delta$ and $m = 1$, relation (14) becomes $\Delta t \le \Delta/(v_{max}\sqrt{2.7}) = 0.86\Delta t_{2D}$. In contrast, in the 3D case, the result is $\Delta t_{3D} \le \Delta/(v_{max}\sqrt{3})$,

which would require more time steps to be executed for any given time period.

B. Source

Several approaches were tried for the simulation of a spatially Gaussian weighted pulse with various time histories. Initially a $(1 - t^2)^4$ time history was used, in combination with a method that essentially imposes a perfect magnetic conductor on the tangential magnetic-field nodes (shorting the fields) and excites the tangential electric-field nodes on the planes on either side of the perfect-magnetic-conductor location; this launches both $+z$ and $-z$ traveling waves. Gaussian spatial weighting [of the form $\exp(-\rho^2/w_0^2)$, where w_0 is the $1/e$ amplitude waist] was then simply enforced at the source points. Testing this method in free space showed that it did indeed generate the expected propagating Gaussian waves but that it also generated a static component in the region of the source, static in both space and time, as a more thorough investigation of the fields in the source region in the late-time part of the problem showed. We believe this to be caused by the nonphysical source model used.

Subsequent research (and all the results given in this paper) used a scattered field–total-field formulation, described in Ref. 11, combined with the first derivative of $(1 - t^2)^4$, i.e., $-8t(1 - t^2)^3$. This waveform was chosen for its zero dc average, smooth turnon and turnoff (both the waveform and its first derivative are zero), and rapid zero crossing behavior. A plane of constant z was selected; the fields on and beyond this plane were total fields, and the fields before this plane were scattered fields. [The specific choice made was the plane j containing only tangential H nodes, i.e., $z = (j_{scat/tot} - 1/2)\Delta z$, with the indexing scheme being as defined in Appendix A.] The FDTD time-marching equations may be used for either the total or the scattered fields; at an interface such as that used here, a simple procedure can be used to ensure consistency of the fields. To update the (total) fields on the interface plane, we require the total fields just before this plane, but only the scattered fields are stored in the computer. We temporarily recover the total field by adding the (known) incident field (with the time history and the Gaussian spatial distribution discussed above) for this update. Similarly, the update for the scattered-field nodes just before this plane requires the scattered fields on the plane; these are recovered by subtraction of the known incident field (suitably retarded in time to be consistent with the discussion given above).

Such modifications to the algorithms are required only for those nodes either on or just before the selected source plane. However, in preparation for a parallel version of the code, the slightly different implementation given below was used. This algorithm uses a modifier array set equal to the desired incident field at the plane $z = (j - 1)\Delta z$ for the tangential E-field modifiers and zero elsewhere; a similar treatment for the tangential H-field modifiers is used, except with the time value being retarded slightly. Note that the incident field is assumed to be entirely transversely polarized; hence no modifiers need be applied to the longitudinal (in this paper, z directed) field components. These equations use the indexing scheme defined in Appendix A:

$$H_{\phi k}{}^{n+1}(i, j) = H_{\phi k}{}^n(i, j) - \frac{\Delta t}{\mu}$$
$$\times \left\{ \frac{E_{\rho k}{}^n(i, j + 1) - [E_{\rho k}{}^n(i, j) + E_{pk}{}^{n'}(i, j)]}{z_0(j + 1) - z_0(j)} \right\}$$
$$+ \frac{\Delta t}{\mu} \left[\frac{E_{zk}{}^n(i + 1, j) - E_{zk}{}^n(i, j)}{\rho_0(i + 1) - \rho_0(i)} \right], \qquad (15)$$

$$B \cdot E_{\rho k}{}^{n+1}(i, j) = A \cdot E_{\rho k}{}^n(i, j) + \frac{k}{\rho(i)} H_{zk}{}^{n+1}(i, j + 1)$$
$$\times \left\{ \frac{[H_{\phi k}{}^{n+1}(i, j + 1) - H_{\phi k}{}^{n+1'}(i, j + 1)] - H_{\phi k}{}^{n+1}(i, j)}{z(j + 1) - z(j)} \right\}$$
$$- J_{\rho k}, \qquad (16)$$

with the modifier arrays being defined as

$$E_{\rho k}{}^{n'}(i, j) = \begin{cases} f(t)\exp(-\rho^2/w_0{}^2) & \text{if } j = j_{scat/tot} \\ 0 & \text{otherwise} \end{cases}, \quad (17)$$

$$H_{\phi k}{}^{n+1'}(i, j) = \begin{cases} f(t - t_r)\exp(-\rho^2/w_0{}^2) & \text{if } j = j_{scat/tot} \\ 0 & \text{otherwise} \end{cases}. \quad (18)$$

Mathematically, this implementation is identical to that described in the previous paragraph (since the modifier arrays are only nonzero on or just below the scattered-field–total-field interface), but this operation is much easier to parallelize in a language such as FORTRAN 90: the branching is now established implicitly by the data instead of explicitly by the code. On a serial machine this would not be an efficient way of coding the algorithm, since a large number of additions and subtractions involving zero are required, but on a parallel system, especially a single-instruction, multiple-data (SIMD) system such as the CM-2, the processors not on the scattered-field–total-field boundary would in any case have to wait for the special treatment of the scattered-field–total-field nodes by the processors assigned to these nodes; hence there is no time penalty in the parallel code for these additional (superfluous) operations. This is an example of the change of mind-set that the new parallel languages are bringing to computational science and engineering (Ref. 12, p. 15).

The time retardation t_r in Eq. (18) must be carefully considered because of the spatial and the temporal offsets between the **E** and the **H** fields in the Yee scheme. The modified **E** fields that are required must be evaluated at time $t_E(n) = (n - 1/2)\Delta t$, whereas the modified **H** fields must be evaluated at time $t_H(n + 1) = n\Delta t$; it appears that the time at which the modified **H** fields are computed should thus be advanced by $\Delta t/2$. However, for the wave to be modeled in a consistent fashion, the $\Delta z/2$ spatial offset of the nodes imposes a $\Delta z/(2c)$ time retardation on the **H** fields for a $+z$ propagating wave (c is the speed of light). Noting the Courant criterion, relation (14), and using the given $m = 1$ form for the uniform spatial discretization of $\Delta t \leq \Delta/(v_{max}\sqrt{2.7})$ or, explicitly, $\Delta t = \xi\Delta/(v_{max}\sqrt{2})$, where $\xi \leq 0.86$, we find that the desired retardation is

$$t_r = \frac{\Delta z}{2c}(1 - \xi/\sqrt{2}). \qquad (19)$$

Note that, in the limit as $\xi \to 0$ (i.e., the time step and hence the time offset between the **E** and the **H** fields becomes negligible), the retardation tends to $\Delta z/(2c)$,

which is simply the time difference caused by the spatial offset. (Of course, if Δz is now also permitted to approach zero, then the retardation tends to zero.)

C. Boundary Conditions

ABC's that permit the simulation of unbounded free space by a bounded computational space have been the topic of active research for well over a decade[3,4]; the challenge is to derive an ABC that will absorb energy over a wide range of incident angles. For the problems investigated in this paper the problem domain must be large enough to contain the Gaussian beam properly, so the difficult problem of developing ABC's that are valid at near-grazing incidence on the side ($\rho = \rho_{max}$) boundaries was circumvented. At the two constant z boundaries ($z = 0$ and $z = z_{max}$) simple first-order ABC's were used.[3] We show the derivation of the one-dimensional ABC at the bottom wall ($z = 0$); the discussion parallels that given in Ref. 3.

An ABC that simulates the incidence of a normally incident plane wave on a perfectly absorbing surface is required. The following (advective) equation has a wave solution $f(z + ct)$ traveling only in the $-z$ direction:

$$\left[\frac{\partial}{\partial z} - \frac{1}{c} \frac{\partial}{\partial t} \right] \phi(z, t) = 0 . \tag{20}$$

Hence imposing this condition on a wave normally incident on the plane surface results in the wave's being absorbed. Thus a suitable ABC is

$$\frac{\partial}{\partial z} \phi(z,t)|_{z=0} = \frac{1}{c} \frac{\partial}{\partial t} \phi(z,t)|_{z=0} . \tag{21}$$

Using forward differencing in space and time, we may approximate this equation as

$$\phi_1{}^n - \phi_0{}^n = \frac{\Delta z}{c\Delta t}(\phi_0{}^{n+1} - \phi_0{}^n) , \tag{22}$$

where $\phi_j{}^n$ is the nth time sample of the field ϕ sampled at the jth spatial sample. This equation may be rewritten to give the desired expression:

$$\phi_0{}^{n+1} = \phi_0{}^n\left(1 - \frac{c\Delta t}{\Delta z}\right) + \frac{c\Delta t}{\Delta z}\phi_1{}^n . \tag{23}$$

In the context of this paper ϕ will be E_ρ and E_ϕ; the ABC must be applied to both tangential components. For the $z = z_{max}$ boundary we may derive a similar expression by using the advective equation for a positively traveling wave and backward differencing in space; the result is

$$\phi_{k_{max}+1}{}^{n+1} = \phi_{k_{max}+1}{}^n\left(1 - \frac{c\Delta t}{\Delta z}\right) + \frac{c\Delta t}{\Delta z}\phi_{k_{max}}{}^n , \tag{24}$$

where k_{max} is the number of samples in the z direction.

These ABC's are accurate to first order since either forward- or backward-differencing schemes are used. (The Yee algorithm, which uses central differencing, is a second-order scheme.) It is possible to derive second-order schemes for the ABC's; an example is given in Ref. 3, Sec. 4.7.1. Only the first-order ABC's given above were used for the research reported here, since the fields are almost normally incident upon the $z = 0$ and the $z = z_{max}$ boundaries, and the minimal reflection from these boundaries did not give rise to any corruption of the results. For all the numerical results shown below, the boundary reflections were smaller than the maximum values by at least 23.5 dB in amplitude.

4. PULSED GAUSSIAN BEAM FIELDS

A. Overview of Pulsed Gaussian Beam Behavior

Consider a thin circular aperture lens of radius a and focal length f in the plane $z = 0$. We assume that this aperture is driven everywhere with the Gaussian spatially tapered, arbitrary-time-signal, pulsed beam:

$$G(\rho, \phi, z, t) = E_0 \exp(-\rho^2/w_0{}^2)F(t) , \tag{25}$$

where the Fourier transform $\bar{F}(\omega)$ is related to the time signal $F(t)$ through the Fourier-transform expressions

$$\bar{F}(\omega) = \int_{-\infty}^{\infty} F(t)\exp(+i\omega t)\mathrm{d}t , \tag{26}$$

$$F(t) = \frac{1}{2\pi} \int_{-\infty}^{\infty} \bar{F}(\omega)\exp(-i\omega t)\mathrm{d}\omega . \tag{27}$$

The Fourier transform of the aperture field is thus simply

$$\tilde{G}(\rho, \phi, z, \omega) = E_0 \exp(-\rho^2/w_0{}^2)\bar{F}(\omega) . \tag{28}$$

The field is then assumed to propagate from the initial aperture into the half-space $z > 0$, which is taken to be a dispersionless, lossless, linear medium.

As demonstrated by Ziolkowski,[13] UWB pulsed beams have propagation properties analogous to monochromatic cw beams. Quantitative bounds on the performance characteristics of UWB pulsed beams associated with multiple-derivative transmitter–receiver array systems have been derived.[7,13] These bounds require the introduction of a set of effective frequencies that characterize by a single frequency value all the broad-bandwidth components contained in all the signals involved in the radiation and measurement processes. For the analysis below, only the basic radiated field behavior of a UWB pulsed beam is required.

If $\mathcal{A}$ is the initial aperture whose area is A, the effective frequency ω_{rad} of a UWB radiated field is given by the expression

$$\omega_{rad}{}^2 \stackrel{\text{def}}{=} \frac{\int_{\mathcal{A}} \mathrm{d}S \int_{-\infty}^{\infty} \mathrm{d}t |\partial G(\mathbf{r}, t)/\partial t|^2}{\int_{\mathcal{A}} \mathrm{d}S \int_{-\infty}^{\infty} \mathrm{d}t |G(\mathbf{r}, t)|^2}$$

$$= \frac{\int_{\mathcal{A}} \mathrm{d}S \int_{-\infty}^{\infty} \mathrm{d}\omega \omega^2 |\tilde{G}(\mathbf{r}, \omega)|^2}{\int_{\mathcal{A}} \mathrm{d}S \int_{-\infty}^{\infty} \mathrm{d}\omega |\tilde{G}(\mathbf{r}, \omega)|^2} . \tag{29}$$

This effective frequency ω_{rad} accounts for the spectral energies launched into the medium in our model, particularly those reaching the far field. For the separable driving signals given in Eq. (25), the effective frequency ω_{rad} reduces simply to the expression

$$\omega_{rad}{}^2 = \frac{\int_{-\infty}^{\infty} \mathrm{d}t |\partial F(t)/\partial t|^2}{\int_{-\infty}^{\infty} \mathrm{d}t |F(t)|^2} = \frac{\int_{-\infty}^{\infty} \mathrm{d}\omega \omega^2 |\bar{F}(\omega)|^2}{\int_{-\infty}^{\infty} \mathrm{d}\omega |\bar{F}(\omega)|^2} . \tag{30}$$

Using the arguments introduced by Ziolkowski et al.[14] and assuming that the observation point is sufficiently

far from the aperture that for any forward-propagating components $(\partial G/\partial z) \sim -[\partial G/\partial(ct)]$, we find that a very good approximation of the field generated by driving a circular aperture $\mathcal{A}$ of radius a in the plane $z = 0$ with the pulsed beam $G(\mathbf{r}, t)$ is

$$g(\mathbf{r}, t) \approx \int_{\mathcal{A}} dS' \left[2 \frac{\partial G(x', y', z' = 0, t')}{\partial(ct')} \right]_{t' = t - R/c} \frac{1}{4\pi R},$$

(31)

where R is the distance between a source point and the observation point. The input energy $\mathcal{E}^{\text{in}}$ along the axis is

$$\mathcal{E}_{\text{in}} = \int_{-\infty}^{\infty} dt |G(\rho = 0, \phi, z = 0, t)|^2,$$

(32)

and the energy radiated along the propagation axis is measured as

$$\mathcal{E}_{\text{rad}}(z) = \int_{-\infty}^{\infty} dt |g(\rho = 0, \phi, z, t)|^2.$$

(33)

The energy efficiency of the aperture-lens system can then be defined as the ratio of the energy radiated along the propagation axis to the energy input along the axis. As shown by Ziolkowski and Judkins[7] for the case of a pulsed Gaussian beam, if

$$L_G = \pi w_0^2 / \lambda_{\text{rad}}$$

(34)

is the Rayleigh distance of the Gaussian beam, the energy efficiency can be obtained from Eq. (31) and satisfies the bound

$$\frac{\mathcal{E}_{\text{rad}}{}^G(z)}{\mathcal{E}_{\text{in}}{}^G} \leq \left(\frac{L_G}{z} \right)^2.$$

(35)

This result is a refinement on the more general UWB pulsed-beam bound[13] that incorporates the effective area of the Gaussian amplitude taper: πw_0^2. Moreover, the waist of the pulsed Gaussian beam can also be described. Let the waist be defined as the transverse width of the energy profile at which it has decreased to $1/e^2$ of its maximum value. As shown by Ziolkowski and Judkins,[7] the energy waist of the pulsed Gaussian beam at z is given approximately as

$$w_{\text{enrg}}(z) \sim \theta_{\text{enrg}}{}^G z \sim \frac{\lambda_{\text{rad}} z}{\pi w_0},$$

(36)

where the beam divergence is explicitly

$$\theta_{\text{enrg}}{}^G \sim \frac{\lambda_{\text{rad}}}{\pi w_0}.$$

(37)

Thus the beam divergence is governed by the effective wavelength and the waist of the initial Gaussian taper.

Also note that the intensity and the energy profiles of a beam behave differently in the general UWB case. They are controlled by different, but related, properties of the spectra of the input field. In general the maximum-intensity (in time) beam width $\theta_{\text{int}}{}^G$ will be narrower than the energy beam width $\theta_{\text{enrg}}{}^G$, i.e.,

$$\theta_{\text{int}}{}^G \leq \theta_{\text{enrg}}{}^G,$$

(38)

because the maximum intensity in time represents an instantaneous rather than an average property of the beam. The equality occurs for any cw case. The resulting narrower-intensity profiles of an UWB system will have significant implications for the focal region of a lens-directed, pulse-driven beam, as is discussed below.

These basic properties of a pulsed beam propagating in free space are used below to guide the analysis of the lens-directed pulsed beam.

B. Pulsed-Beam Behavior in the Focal Region of a Lens

If a thin lens is introduced in the initial aperture, one can represent the effects of the lens by introducing into the frequency-domain version of Eq. (31) the transfer function

$$T_{\text{lens}}(\rho, \phi, z, \omega) = \exp\left(-i \frac{\omega \rho^2}{2cf} \right).$$

(39)

One then obtains

$$g(\mathbf{r}, t) \approx \frac{1}{2\pi} \int_{-\infty}^{\infty} d\omega \int_{\mathcal{A}} dS' \, T_{\text{lens}}(\mathbf{r}, \omega) \left(\frac{-2i\omega}{c} \right)$$
$$\times \tilde{G}(\mathbf{r}, \omega) \frac{\exp[-i\omega(t - R/c)]}{4\pi R}.$$

(40)

Thus, if the driving function is the pulsed beam given by Eq. (25), then one can represent the lens-directed pulsed-beam field in the region $z > 0$ simply by using the Fourier-transform domain expression, relation (40), and the Fourier-transform derivative property to obtain

$$g(\mathbf{r}, t) \approx \frac{1}{2\pi} \int_{-\infty}^{\infty} d\omega \tilde{F}(\omega) \int_0^{2\pi} d\phi'$$
$$\times \int_0^a d\rho' \rho' \exp[-i(\omega/c)(\rho'^2/2f)]$$
$$\times \frac{1}{4\pi R} \left\{ E_0 \left(\frac{-2i\omega}{c} \right) \exp(-\rho'^2/w_0^2) \right.$$
$$\times \left. \exp[-i\omega(t - R/c)] \right\}$$
$$= 2 \frac{E_0}{2\pi c} \frac{\partial}{\partial t} \int_{-\infty}^{\infty} d\omega \tilde{F}(\omega)$$
$$\times \int_0^{2\pi} d\phi' \int_0^a d\rho' \rho' \exp[-i(\omega/c)(\rho'^2/2f)]$$
$$\times \left\{ \exp(-\rho'^2/w_0^2) \frac{\exp[-i\omega(t - R/c)]}{4\pi R} \right\}.$$

(41)

Since for $z \gg \rho$, $z \gg \rho'$ the distance term

$$R = [\rho^2 + \rho'^2 - 2\rho\rho' \cos(\phi - \phi') + z^2]^{1/2}$$
$$\sim z + \frac{\rho^2 + \rho'^2}{2z} - \frac{\rho\rho'}{z} \cos(\phi - \phi'),$$

(42)

one has approximately, with the standard integral representation of the zeroth-order Bessel function,

$$g(\mathbf{r}, t) \approx \frac{E_0}{2\pi c z} \frac{\partial}{\partial t} \int_{-\infty}^{\infty} d\omega \tilde{F}(\omega) \exp[-i\omega(t - z/c)]$$
$$\times \exp[+i(\omega/c)(\rho^2/2z)]$$
$$\times \int_0^a d\rho' \rho' \exp[-i(\omega/c)(\rho'^2/2f)]$$
$$\times \exp[+i(\omega/c)(\rho'^2/2z)] \exp(-\rho'^2/w_0^2)$$
$$\times \frac{1}{2\pi} \int_0^{2\pi} d\phi' \exp[+i(\omega/c)(\rho\rho'/z)\cos(\phi - \phi')]$$
$$= \frac{E_0}{2\pi c z} \frac{\partial}{\partial t} \int_{-\infty}^{\infty} d\omega \tilde{F}(\omega) \exp[-i\omega(t - z/c)]$$
$$\times \exp[+i(\omega/c)(\rho^2/2z)]$$
$$\times \int_0^a d\rho' \rho' \exp(-\rho'^2/w_0^2)$$
$$\times \exp\left[-i\left(\frac{\omega}{c} \right)\left(\frac{1}{z} - \frac{1}{f} \right)\left(\frac{\rho'^2}{2} \right) \right] J_0\left(\frac{\omega}{c} \frac{\rho}{z} \rho' \right).$$

(43)

This expression represents the field behavior both on and near the axis of the lens.

We calculate the on-axis behavior of the lens-directed pulsed beam from Eq. (43) by setting $\rho = 0$. This gives

$$
\begin{aligned}
g(\rho = 0, \phi, z, t) &\approx \frac{E_0}{2\pi c z} \frac{\partial}{\partial t} \int_{-\infty}^{\infty} d\omega \tilde{F}(\omega) \\
&\times \exp[-i\omega(t - z/c)] \\
&\times \int_0^a d\rho' \rho' \exp[-(\Lambda/\omega_0^2)\rho'^2] \\
&= E_0 \frac{w_0^2}{2cz} \frac{\partial}{\partial t} \int_{-\infty}^{\infty} \frac{d\omega}{2\pi} \tilde{F}(\omega) \\
&\times \exp[-i\omega(t - z/c)] \\
&\times \frac{1 - \exp[-(a/w_0)^2 \Lambda]}{\Lambda} \\
&= E_0 \frac{L_G}{z} \frac{1}{\omega_{\text{rad}}} \frac{\partial}{\partial t} \int_{-\infty}^{\infty} \frac{d\omega}{2\pi} \tilde{F}(\omega) \\
&\times \exp[-i\omega(t - z/c)] \\
&\times \frac{1 - \exp[-(a/w_0)^2 \Lambda]}{\Lambda},
\end{aligned} \tag{44}
$$

where the term

$$
\Lambda = 1 - i\frac{\omega w_0^2}{2c}\left(\frac{1}{z} - \frac{1}{f}\right) = 1 - i\frac{\omega}{\omega_{\text{rad}}} L_G\left(\frac{1}{z} - \frac{1}{f}\right) \tag{45}
$$

has been introduced. The presence of the time derivative indicates that pulses with larger rise times will generate larger fields in the focal regions.

Although Eq. (44) cannot be evaluated analytically for arbitrary spectra, one could obtain numerical results simply by using a fast-Fourier-transform (FFT) routine. In particular, one could investigate in this manner the focal shift (displacement of the focus from $z = f$ toward the lens) as a function of the bandwidth, the rise time, etc. of the driving-time signal $F(t)$. On the other hand, it is possible to obtain an approximate expression that reveals some of the related behavior before the focal plane is reached. Near the focal plane the imaginary term in Λ should contribute mainly to the phase. We can approximate the integrand, evaluate the integrals, and use a Taylor expansion to obtain

$$
\begin{aligned}
g(\rho = 0, \phi, z, t) &\sim E_0 \frac{L_G}{z} \frac{1}{\omega_{\text{rad}}} \frac{\partial}{\partial t} \int_{-\infty}^{\infty} \frac{d\omega}{2\pi} \tilde{F}(\omega) \\
&\times \exp[-i\omega(t - z/c)] \\
&\times \{1 - \exp[-(a/w_0)^2]\Lambda\} \\
&\sim E_0 \frac{L_G}{z} \frac{1}{\omega_{\text{rad}}} \{1 - \exp[-(a/w_0)^2]\} \\
&\times \frac{\partial}{\partial t} F(t - z/c) \\
&+ E_0 \frac{L_G L_R}{z}\left(\frac{1}{z} - \frac{1}{f}\right) \exp[-(a/w_0)^2] \\
&\times \frac{1}{\omega_{\text{rad}}^2} \frac{\partial^2}{\partial t^2} F(t - z/c),
\end{aligned} \tag{46}
$$

where $L_R = A/\lambda_{\text{rad}}$ is the Rayleigh distance of the aperture when it is driven with a uniform transverse amplitude distribution. In the UWB case the second-derivative terms can be quite large. Thus there may be significant modifications of the field in the region just before the focal plane in the UWB case. Note that when $a \gg w_0$ this additional term is negligible.

On the other hand, one can obtain an explicit analytical expression at the focal plane where $z = f$, so that $\Lambda = 1$. One obtains

$$
\begin{aligned}
g(\rho = 0, \phi, z = f, t) &\sim E_0 \frac{L_G}{f} \frac{1}{\omega_{\text{rad}}} \\
&\times \frac{\partial}{\partial t} \int_{-\infty}^{\infty} \frac{d\omega}{2\pi} \tilde{F}(\omega) \exp[-i\omega(t - f/c)] \\
&\times \{1 - \exp[-(a/w_0)^2]\} \\
&= E_0 \frac{L_G}{f} \frac{1}{\omega_{\text{rad}}} \{1 - \exp[-(a/w_0)^2]\} \\
&\times \frac{\partial}{\partial t} F(t - f/c).
\end{aligned} \tag{47}
$$

Thus, in general agreement with Sherman[15] and Bor and Horváth,[16] the behavior of the lens-directed pulsed beam at the focus depends on a retarded time derivative of the initial signal. Similarly, in analogy with known time-harmonic results,[17,18] the behavior of a pulsed beam at the focus of a thin lens should reflect its far-field behavior. The appearance of the time derivative in the far-field behavior of a pulsed beam has been established.[7,13] In comparing relation (47) with relation (46), one finds that only the first term of relation (46) remains as expected.

More explicit statements can be obtained from relation (47). Note that for driving fields that are separable in space and time, such as in Eq. (25), many of the UWB expressions simplify. One can introduce the focal amplification factor $\mathcal{F}\mathcal{A}_{\text{enrg}}$ as the energy received at the focus to the input energy. From relation (47) one obtains

$$
\mathcal{F}\mathcal{A}_{\text{enrg}} \stackrel{\text{def}}{=} \frac{\mathcal{E}_{\text{rad}}(f)}{\mathcal{E}_{\text{input}}} = \{1 - \exp[-(a/w_0)^2]\}^2\left(\frac{L_G}{f}\right)^2. \tag{48}
$$

Similarly, one can introduce a focal amplification factor $\mathcal{F}\mathcal{A}_{\text{int}}$ for the ratio of the maximum field intensity on axis in time to its maximum initial value. Let the symbol $\max_t u(t)$ represent the operation of finding the maximum in time of the function $u(t)$. From relation (47) one obtains

$$
\begin{aligned}
\mathcal{F}\mathcal{A}_{\text{int}} &\stackrel{\text{def}}{=} \frac{\max_t |g(\rho = 0, \phi, z = f, t)|^2}{\max_t |G(\rho = 0, \phi, z = 0, t)|^2} \\
&\sim \{1 - \exp[-(a/w_0)^2]\}^2\left(\frac{L_G}{f}\right)^2 \\
&\times \frac{[\max_t |\partial F(t - f/c)/\partial t|^2]}{\omega_{\text{rad}}^2} \\
&= \Upsilon_{\text{int}} \times \mathcal{F}\mathcal{A}_{\text{enrg}},
\end{aligned} \tag{49}
$$

where we have introduced the intensity-enhancement (IE) factor

$$
\Upsilon_{\text{int}} = \frac{[\max_t |\partial F(t - f/c)/\partial t|^2]}{\omega_{\text{rad}}^2} \equiv \frac{[\max_t |\partial F(t)/\partial t|^2]}{\omega_{\text{rad}}^2}. \tag{50}
$$

The IE factor clearly indicates that one can use UWB driving signals to achieve a larger IE than is possible with equivalent cw signals.

In particular, if $F(t)$ represents a monochromatic signal with $\omega = \omega_{\mathrm{rad}}$, then one finds that at the focus the cw and the UWB energy focal amplification factors are identical:

$$\mathcal{F}\mathcal{A}_{\mathrm{enrg}}{}^{\mathrm{cw}} = \mathcal{F}\mathcal{A}_{\mathrm{enrg}}{}^{\mathrm{UWB}} \sim \left(\frac{L_G}{f}\right)^2, \qquad (51)$$

where the last expression is most appropriate for cases in which $w_0 \ll a$ and agrees with known cw results.[17,18] In particular, if $f < L_G$, one achieves an enhancement of the energy at the focus. Relation (51) indicates that, for the same input energy, the energy delivered (over time) at the focus of a thin lens is approximately the same in the cw and the UWB cases. However, the cw IE factor $\Upsilon_{\mathrm{int}}{}^{\mathrm{cw}} \equiv 1$. Therefore the cw and the UWB maximum beam intensities at the focus satisfy

$$\frac{\mathcal{F}\mathcal{A}_{\mathrm{int}}{}^{\mathrm{UWB}}}{FA_{\mathrm{int}}{}^{\mathrm{cw}}} = \frac{[\max_t |\partial F_{\mathrm{UWB}}(t)/\partial t|^2]}{\omega_{\mathrm{rad}}{}^2} = \Upsilon_{\mathrm{int}}{}^{\mathrm{UWB}}. \qquad (52)$$

Thus, depending on the design of the driving-time signal, one could obtain a significant intensity enhancement in the UWB case.

We return now to the field expression, relation (43). The radial behavior of the lens-directed pulsed beam in the focal plane $z = f$ follows immediately. Using [Ref. 19, Eq. (6.631.4)]

$$\int_0^\infty \mathrm{d}x \ \exp(-\alpha x^2) J_0(\beta x) = \frac{\exp(-\beta^2/4\alpha)}{2\alpha} \quad (\mathrm{Re}\ \alpha > 0), \qquad (53)$$

one can evaluate the integral in relation (43) in closed form with a remainder term that can be bounded, since $\Lambda = 1$ when $z = f$. One obtains

$$\int_0^a \mathrm{d}\rho'\rho' \ \exp[-(\rho'/w_0)^2] J_0\left(\frac{\omega}{c}\frac{\rho}{f}\rho'\right)$$

$$= \frac{1}{2} \exp\left\{-\frac{1}{4}\left[\left(\frac{\omega}{cz}\right)^2\right]\rho^2\right\}$$

$$- \int_a^\infty \mathrm{d}\rho'\rho' \ \exp[-(\rho'/w_0)^2] J_0\left(\frac{\omega}{c}\frac{\rho}{f}\rho'\right). \qquad (54)$$

For the cases considered below, we assume that $a > w_0$, which causes the exponential term in the remainder integral in Eq. (54) to be small. Moreover, for off-axis points the argument of the Bessel function is large, i.e., it is at least $(\omega/c)(\rho a/f) = 2(\pi a^2/\lambda f)(\rho/a) < 2(\pi a^2/\lambda_{\mathrm{rad}}f)(\rho/a) = 2(L_G/f)(a/w_0)^2(\rho/a)$ in size for the wavelengths of interest; this is large since f is taken to be in the near field of the pulsed beam. The Bessel function will then be highly oscillatory, resulting in a small value for the integral. With this behavior, relation (43) reduces in the focal plane to the expression

$$g(\rho, \phi, z = f, t) \approx E_0 \frac{L_G}{f} \frac{1}{\omega_{\mathrm{rad}}} \frac{\partial}{\partial t} \int_{-\infty}^\infty \frac{\mathrm{d}\omega}{2\pi} \tilde{F}(\omega)$$

$$\times \exp[-i\omega(t - f/c - \rho^2/2cf)]$$

$$\times \exp[-\omega^2(w_0\rho/2cf)^2]$$

$$= E_0 \frac{L_G}{f} \frac{1}{\omega_{\mathrm{rad}}} \frac{\partial}{\partial t} F(t - f/c - \rho^2/2cf)$$

$$*_t \left(\frac{\sqrt{\pi}}{t} \exp\left\{-(w_{\mathrm{rad}}t)^2\left[\left(\frac{L_G}{f}\right)\left(\frac{\rho}{w_0}\right)\right]^{-2}\right\}\right), \qquad (55)$$

where $*_t$ represents a time convolution and we have used [Ref. 19, Eq. (3.462.3)]

$$\int_{-\infty}^\infty \mathrm{d}x \ \exp(-iax)\exp(-\beta^2 x^2) = \frac{\sqrt{\pi}}{\alpha} \ \exp(-\alpha^2/4\beta^2). \qquad (56)$$

Notice that very near the axis where $(L_G/f)(\rho/w_0) \ll 1$ the term given inside the boldface parentheses in relation (55) acts as a delta function, and one obtains

$$g(\rho, \phi, z = f, t) \approx E_0 \frac{L_G}{f} \frac{1}{\omega_{\mathrm{rad}}} \frac{\partial}{\partial t} F(t - f/c - \rho^2/2cf), \qquad (57)$$

which is only slightly different from the on-axis value of relation (47). On the other hand, further off axis the term $(L_G/f)(\rho/w_0)$ is not small, which means the convolution term will begin to broaden the field distribution. This means that the waist $w(f)$ of the pulsed beam in the focal plane must satisfy

$$w(f) \le \left(\frac{f}{L_G}\right) w_0 = \theta_{\mathrm{enrg}}{}^G f, \qquad (58)$$

where $\theta_{\mathrm{enrg}}{}^G$ is as defined in relation (37). The upper bound indicated by this relation agrees essentially with known cw expressions.[17,18]

C. Intensity-Enhancement-Pulse Design

It is clear from Eq. (52) that IE's between the UWB and the cw cases can be achieved. In essence, one must increase the ratio of the maximum radiated intensity over time to the average radiated intensity in time (radiated energy). The process by which this can be achieved is illustrated with two simple analytical examples.

The first example is the piecewise-linear time signal

$$F_{\mathrm{PL}}(t) = \begin{cases} t/T_1 & \text{for } 0 \le t \le T_1 \\ 1 - 2(t - T_1)/(T_2 - T_1) & \text{for } T_1 \le t \le T_2 \\ (t - T_3)/(T_3 - T_2) & \text{for } T_2 \le t \le T_3 \end{cases}. \qquad (59)$$

This signal increases linearly from 0 to 1 in the time T_1, decreases linearly from $+1$ to -1 in the time $T_2 - T_1$, and then increases from -1 to 0 in the time $T_3 - T_2$. It has the discontinuous time derivative

$$\frac{\partial}{\partial t} F_{\mathrm{PL}}(t) = \begin{cases} 1/T_1 & \text{for } 0 \le t \le T_1 \\ -2/(T_2 - T_1) & \text{for } T_1 \le t \le T_2 \\ 1/(T_3 - T_2) & \text{for } T_2 \le t \le T_3 \end{cases}. \qquad (60)$$

If we set $T_1 = m\delta$, $T_2 - T_1 = \delta$, and $T_3 - T_2 = m\delta$, so that $T_3 = (2m + 1)\delta$, we find that

$$\int_{-\infty}^\infty \mathrm{d}t |F_{\mathrm{PL}}|^2 = \frac{T_3}{2} = \left(m + \frac{1}{2}\right)\delta, \qquad (61)$$

$$\int_{-\infty}^\infty \mathrm{d}t \left|\frac{\partial}{\partial t} F_{\mathrm{PL}}\right|^2 = \frac{1}{T_1} + \frac{4}{T_2 - T_1} + \frac{1}{T_3 - T_2}$$

$$= \left(4 + \frac{2}{m}\right)\frac{1}{\delta}, \qquad (62)$$

$$\max_t \left|\frac{\partial}{\partial t} F_{\mathrm{PL}}\right|^2 = \frac{4}{\delta^2}, \qquad (63)$$

$$\omega_{\mathrm{rad,PL}}{}^2 = \frac{4}{m} \frac{1}{\delta^2} = \frac{4}{\Upsilon_{\mathrm{int}}{}^{\mathrm{PL}}} \frac{1}{\delta^2}, \qquad (64)$$

$$\Upsilon_{\mathrm{int}}{}^{\mathrm{PL}} = m. \qquad (65)$$

Thus we can design the size of the enhancement and achieve a specified effective radiated frequency by choosing the positive-to-negative switch time δ. For instance, if we choose $\delta = 0.15$ fs and the enhancement factor $\Upsilon_{int}^{PL} = 120$, the frequency $\omega_{rad,PL}^2 = 1.481 \times 10^{30}$, so that the effective wavelength $\lambda_{rad,PL} = 1.549$ μm and the signal record length $T \equiv T_3 = 36.15$ fs.

Another example is the trapezoidal signal

$$F_{TR}(t) = \begin{cases} t/T_1 & \text{for } 0 \le t \le T_1 \\ 1.0 & \text{for } T_1 \le t \le T_2 \\ 1 - 2(t - T_2)/(T_3 - T_2) & \text{for } T_2 \le t \le T_3 \\ -1.0 & \text{for } T_3 \le t \le T_4 \\ (t - T_5)/(T_5 - T_4) & \text{for } T_4 \le t \le T_5 \end{cases} \tag{66}$$

It has the discontinuous time derivative

$$\frac{\partial}{\partial t} F_{TR}(t) = \begin{cases} 1/T_1 & \text{for } 0 \le t \le T_1 \\ 0.0 & \text{for } T_1 \le t \le T_2 \\ -2/(T_2 - T_1) & \text{for } T_2 \le t \le T_3 \\ 0.0 & \text{for } T_3 \le t \le T_4 \\ 1/(T_5 - T_4) & \text{for } T_4 \le t \le T_5 \end{cases} \tag{67}$$

Again, if we set $T_1 = n\delta$, $T_2 - T_1 = m\delta$, $T_3 - T_2 = \delta$, $T_4 - T_3 = m\delta$, and $T_5 - T_4 = n\delta$, so that $T_5 = (2m + 2n + 1)\delta$, we find that

$$\int_{-\infty}^{\infty} dt |F_{TR}|^2 = \frac{1}{2}(2n + 1)\delta + 2m\delta$$

$$= \left(2m + \frac{2n + 1}{2}\right)\delta, \tag{68}$$

$$\int_{-\infty}^{\infty} dt \left| \frac{\partial}{\partial t} F_{TR} \right|^2 = \frac{1}{T_1} + \frac{4}{T_2 - T_1} + \frac{1}{T_3 - T_2}$$

$$= \left(4 + \frac{2}{n}\right)\frac{1}{\delta}, \tag{69}$$

$$\max_t \left| \frac{\partial}{\partial t} F_{TR} \right|^2 = \frac{4}{\delta^2}, \tag{70}$$

$$\omega_{rad,TR}^2 = \frac{4}{\Upsilon_{int}^{TR}} \frac{1}{\delta^2}, \tag{71}$$

$$\Upsilon_{int}^{TR} = 4.0 \frac{2m + (2n + 1)/2}{4 + 2/n}$$

$$= \frac{2m + (2n + 1)/2}{1 + 1/2n}. \tag{72}$$

Again, we can design the size of the enhancement and achieve a specified effective radiated frequency by choosing the positive-to-negative switch time δ. For instance, if we choose $\delta = 0.15$ fs, $m = 50$, and $n = 22$, the frequency $\omega_{rad,TR}^2 = 1.484 \times 10^{30}$, so that the effective wavelength $\lambda_{rad,TR} = 1.547$ μm, the signal record length $T \equiv T_5 = 21.75$ fs, and the enhancement factor $\Upsilon_{int}^{TR} = 119.78$. The differences in the piecewise-linear and the trapezoidal pulse results are minimal. However, they indicate how we could construct a smoother pulse for use in the FDTD code.

Based on these examples, a more continuous pulse that mimics their properties was constructed. The additional smoothness is required for prevention of extraneous noise in the FDTD results. This IE pulse is given by the expressions

$$F_{IE}(t) = \begin{cases} -(1 - x^2)^4, & x = -1.0 + t/T_1 \\ & \text{for } 0 \le t \le T_1 \\ -1 + 2(1 - x^2)^4, & x = (t - T_2)/(T_2 - T_1) \\ & \text{for } T_1 \le t \le T_2 \\ (1 - x^2)^4, & x = (t - T_2)/(T_3 - T_2) \\ & \text{for } T_2 \le t \le T_3 \end{cases} \tag{73}$$

It has the continuous time derivative

$$\frac{\partial}{\partial t} F_{IE}(t)$$

$$= \begin{cases} [8/T_1]x(1 - x^2)^3, & x = -1.0 + t/T_1 \\ & \text{for } 0 \le t \le T_1 \\ -[16/(T_2 - T_1)]x(1 - x^2)^3, & x = (t - T_2)/(T_2 - T_1) \\ & \text{for } T_1 \le t \le T_2 \\ -[8/(T_3 - T_2)]x(1 - x^2)^3, & x = (t - T_2)/(T_3 - T_2) \\ & \text{for } T_2 \le t \le T_3 \end{cases} \tag{74}$$

If we set $T_1 = m\delta$, $T_2 - T_1 = \delta$, and $T_3 - T_2 = m\delta$, so that $T_3 = (2m + 1)\delta$, we find numerically that for $\delta = 0.25$ fs and $m = 88$ the effective frequency $\omega_{rad,IE}^2 = 1.752 \times 10^{30}$, so that $\lambda_{rad,IE} = 1.412$ μm, the time record length $T \equiv T_3 = 44.25$ fs, and the IE factor $\Upsilon_{int}^{IE} = 131.93$. Below we refer to this as the UWB1 case. Thus we can achieve a more than 100-fold increase in the IE factor with a properly designed UWB pulse. Similarly, if we set $\delta = 3.0$ fs and $m = 15$, the effective frequency $\omega_{rad,IE}^2 = 6.564 \times 10^{28}$, so that $\lambda_{rad,IE} = 7.357$ μm; the time record length $T \equiv T_3 = 93.0$ fs, and the IE factor $\Upsilon_{int}^{IE} = 24.5$. Below we refer to this as the UWB2 case. The reason we have modeled both cases numerically is that the former was rather challenging for the BOR-FDTD simulator in terms of our available computer resources.

D. Cases for Numerical Comparisons

Several standard test cases and another specially designed pulse were utilized to compare the analytical results derived above and the numerical results. In particular, we investigated the causal time signals

$$F_{CW}(t) = [1 - x(t)^2]^4 \times \sin[m(2\pi t/T)]$$
$$\text{(windowed cw)}, \quad (75)$$

$$F_{SC}(t) = -(16/T)x(t)[1 - x(t)^2]^3 \quad \text{(single cycle)}, \quad (76)$$

$$F_{UWB3}(t) = -(16/T)x(t)[1 - x(t)^2]^3 \times \{1 + [\beta x(t)]^2\}^{-\alpha}$$
$$\times \left(1 + 0.25\alpha\beta^2[1 - x(t)^2]\{1 + [\beta x(t)]^2\}^{-1}\right)$$
$$\text{(UWB3)}, \quad (77)$$

defined over the interval $[0, T]$, where the term

$$x(t) = 1 - 2(t/T). \tag{78}$$

As with the IE pulses UWB1 and UWB2, these signals are all characterized by being continuous and having continuity in their first two derivatives at the end points of
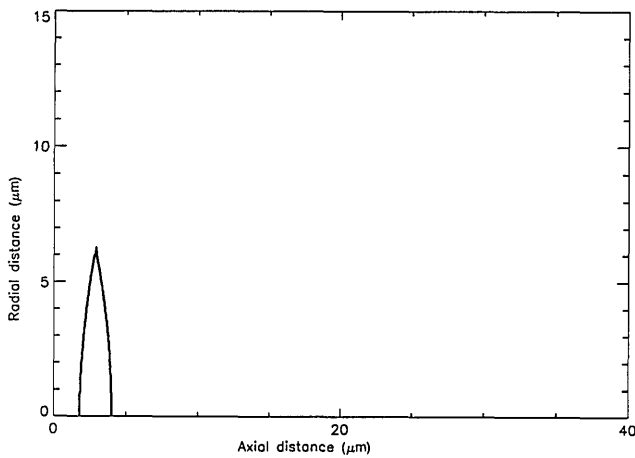
Fig. 1. The lens used in the numerical simulations was double parabolic and thin. For all the cases the lens is located at $z = 3.0$ μm, it is 2.25 μm thick at its base, and its index of refraction is $n = 2$. For the $F_\# = 1.0$ cases the focal length $f = 18.0$ μm and the diameter $D = 18.0$ μm. For the $F_\# = 0.707$ case $f = 9.0$ μm and $D = 12.732$ μm.

the time interval over which they are defined. The signal $F_{cw}(t)$ represents a windowed cw signal and allows one to study the effect of increasing the number of oscillations. If m is the number of cycles in the interval T and T_{cycle} is the period of each cycle, then $T = mT_{cycle}$. In our investigation each cycle was chosen to be 6.0 fs long, so that, for instance, the 10-cycle pulse was 60.0 fs in duration. This gave $\lambda_{rad}^{10\text{-cycle}} = 1.7956$ μm and $Y_{int}^{10\text{-cycle}} = 0.996$. The signal $F_{SC}(t)$ represents a simple, single-cycle pulse; the pulse duration was chosen to be 6.0 fs. This gave $\lambda_{rad}^{1\text{-cycle}} = 1.539$ μm and $Y_{int}^{1\text{-cycle}} = 1.308$. The signal $F_{UWB3}(t)$ represents another designed signal that produces modest enhancements in the IE factor, but it has more structure in its time history and hence presents another challenging case for the BOR-FDTD simulator. The parameters $\alpha = 0.08$ and $\beta = 100.0$ with a pulse duration of $T = 100.0$ fs were used. This gave $\lambda_{rad}^{UWB3} = 2.714$ μm and $Y_{int}^{UWB3} = 9.87$.

5. RESULTS

The lens used in the numerical simulations was double parabolic and thin. For all the cases the lens was located at $z = 3.0$ μm, its thickness at its base was $d = 2.25$ μm, and its index of refraction was $n = 2$. The source plane was located at $z = 1.0$ μm. Two $F_\#$ cases were run, with each having the waist (transverse width, where the $1/e$ value of the amplitude occurs) of the initial pulsed beam set equal to 6.0 μm. The first case, referred to as the $F_\# = 0.707$ case, has the lens radius $a = 6.366$ μm, which is only slightly larger than the waist. The initial pulsed beam thus extends beyond the edge of the lens and will create a strong edge-diffracted pulsed beam. The focal length $f = 9.0$ μm in this case is obtained with the lens equation

$$f = \frac{a^2}{2d(n-1)}. \tag{79}$$

The focal region is thus expected to be centered around $z = 12.0$ μm. The second case, referred to as the $F_\# = 1.0$ case, has the lens radius $a = 9.0$ μm, which is considerably larger than the initial waist. The initial pulsed beam thus interacts very weakly with the edge of the lens and will create a negligible edge-diffracted pulsed beam. The focal length is $f = 18.0$ μm, and the focal region is thus expected to be centered around $z = 21.0$ μm. The basic lens configuration for the $F_\# = 0.707$ case is shown in Fig. 1.

The lens-focused pulsed beams that we generated by driving the aperture with the various time histories discussed in Subsections 4.C and 4.D were studied numerically with the BOR-FDTD simulator. The typical problem involved 300×600 grid cells with $\Delta z = \Delta r = 0.05$ μm. We ran the code for 1200 time steps at 97% of the Courant limit by setting $\Delta t = 0.0978$ fs. The total simulation considered a 15 μm $\times$ 30 μm region in free space and a total time duration of ≈ 118 fs. The average run took 30 min on a CONVEX C-240 computer in a typical multiuser environment. Some runs required a slightly longer run time (such as
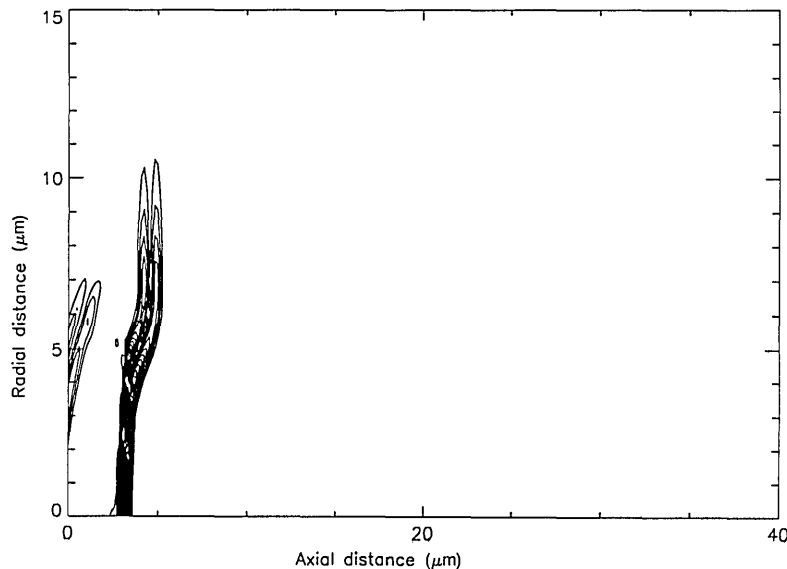

Fig. 2. Contour plot of the E_ρ-field distribution at the time step $n = 150$ for the 1-cycle, $F_\# = 0.707$ case. The pulsed beam is mainly interacting with the lens at this time. Some energy has already been reflected from the front face of the lens. The relative sizes of the beam waist and the lens radius are apparent.
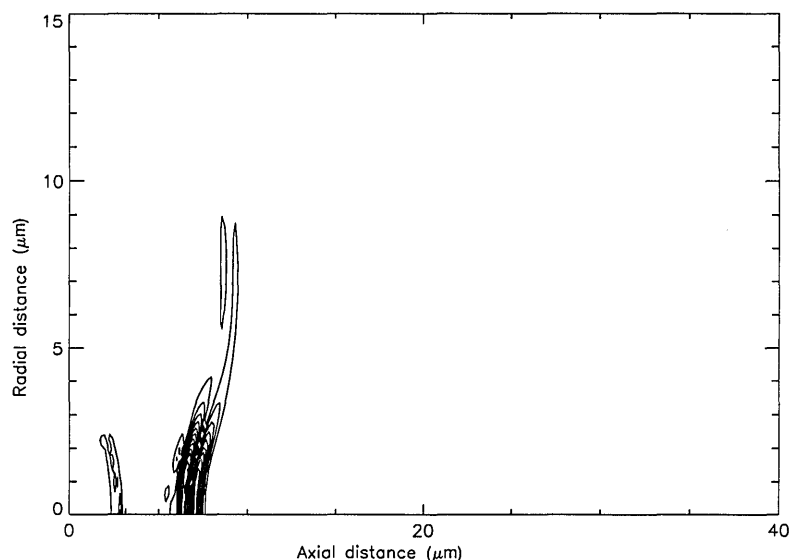
Fig. 3. Contour plot of the E_ρ-field distribution at the time step $n = 300$ for the 1-cycle, $F_\# = 0.707$ case. The pulsed beam has passed through the lens and is now focusing. The change in curvature of the wave fronts caused by the interaction of the pulsed beam with the lens is apparent.
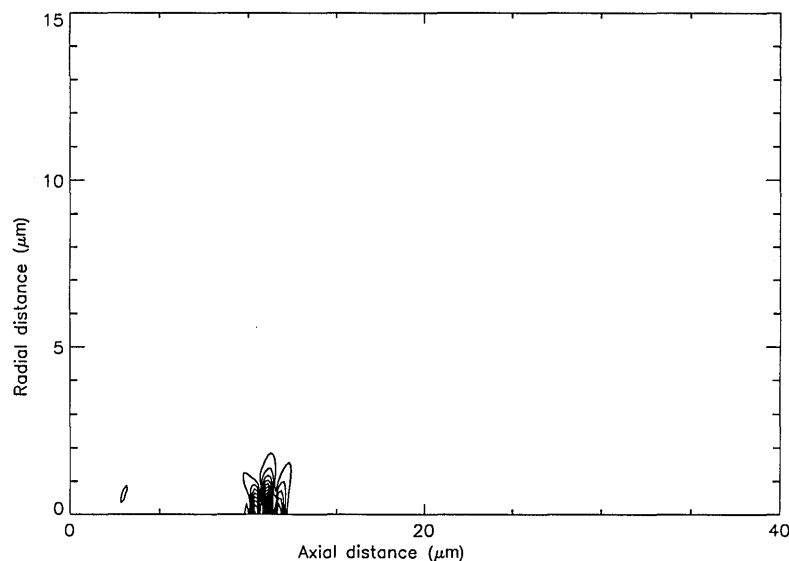

Fig. 4. Contour plot of the E_ρ-field distribution at the time step $n = 450$ for the 1-cycle, $F_\# = 0.707$ case. The pulsed beam is at the focus. The decrease in the beam waist and the time derivative of the field are immediately apparent.

the 10-cycle case, for which 1500 time steps were needed). Certain of the UWB pulses were run at higher discretizations, noted in Tables 1 and 2 below: the 0.0125-μm case used a 1200 × 2400 grid, with 5100 time steps, and required almost 2 1/2 days of clock time to run. The actual CPU time was 958 min at a rate of approximately 18 Mflops/s. Note that the CM-2 runs discussed above ran at an average throughput of approximately 50 Mflops/s.

The BOR-FDTD simulator results include all the field-component time histories at all the points in the mesh. This allows one to observe the time evolution of the pulsed beam as it propagates through the lens and into the focal region. Using the $F_\# = 0.707$ case as an example, we illustrate in Figs. 2–5 the behavior of the lens-focused pulsed beam with contour plots of the intensity corresponding to the transverse field component E_ρ at different

times in the simulation. The initial time history is the single-cycle signal defined by Eq. (76). There are 15 contour levels between the highest and the lowest value of the intensity $|E_\rho|^2$ in each plot. The lens is situated near the source plane, so that the pulsed beam propagates essentially distortion free until it interacts with the lens. Figure 2 shows the field distribution at the $n = 150$ time step when the initial field is strongly interacting with the lens. This figure also includes part of the wave that is reflected from the front face of the lens. It illustrates how well the ABC works on the left boundary; the fields reflected back into the simulation space from that boundary are at least 23.5 dB smaller than the peak values. The presence of both fields is possible since the field in the lens is propagating at half the speed at which it would propagate in free space. The creation of an edge-diffracted wave field is also apparent as the portion of the pulsed
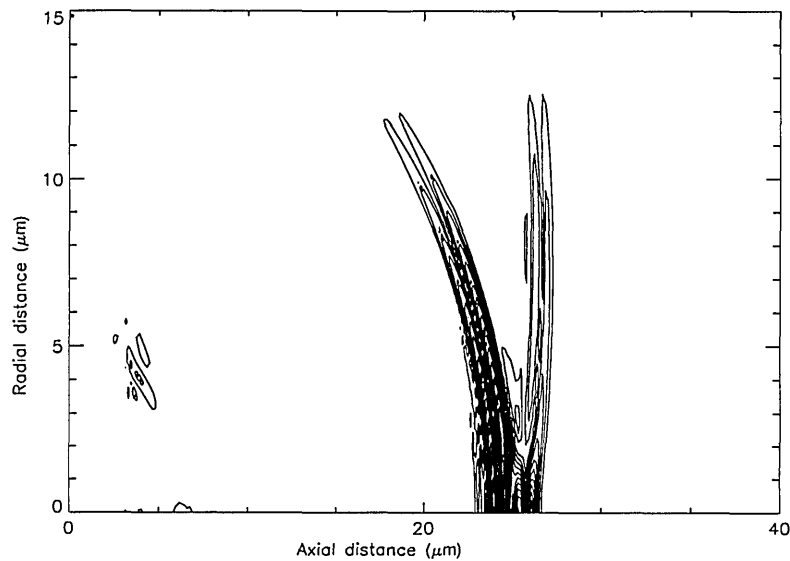
Fig. 5.   Contour plot of the E_ρ-field distribution at the time step $n = 900$ for the 1-cycle, $F_\# = 0.707$ case.   The pulsed beam is well beyond the focus.   The increase in the beam waist, the change in the wave-front curvature, and the leading wave front caused by the edge of the lens are readily identifiable.
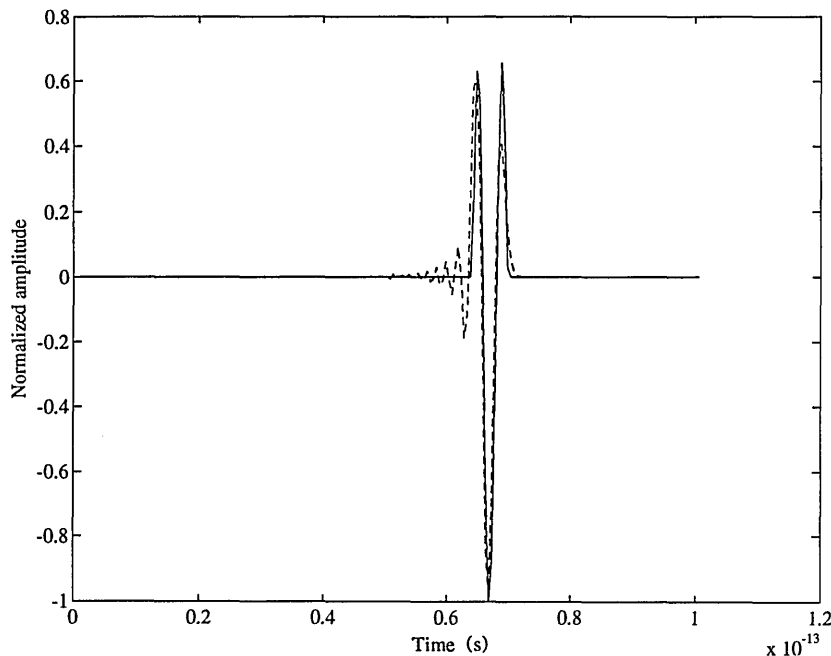

Fig. 6.   Signal along the propagation axis at the focus should be nearly the time derivative of the original source signal.   The FDTD numerically generated signal at the focus is compared with the time derivative of the source signal.   Solid curve, time derivative of the source signal; dashed curve, FDTD-computed pulse.

beam in free space speeds past the lens.   Figure 3 shows the transverse electric-field intensity distribution as the pulsed beam has propagated beyond the lens.   This is taken at the time step $n = 300$.   Note the curvature of the wave fronts induced by the lens toward the focal region.   The focus is reached at the time step $n = 450$. The intensity distribution in this focus region is shown in Fig. 4.   The expected time-derivative behavior of the field and the decrease in the waist size are apparent. After it has reached the focus the pulsed beam begins to expand once more.   This is illustrated in Fig. 5, where the intensity distribution is given for the time step $n = 900$.   The beam is well beyond the focus.   Note that the

curvature is appropriate for a field expanding away from a focal region.   Also note that there is a field distribution that has appeared on the leading edge of the pulsed beam.   This is the edge-diffracted field reported by Bor and Horváth.[16]   It is essentially a Bessel beam arising from the field distribution in the immediate vicinity of the edge of the lens.   Since it is always traveling in free space, this beam propagates slightly ahead of the main beam, which interacted with the center of the dielectric lens.

The analytical results given in Subsection 4.B indicate that the pulsed beam should have a time-derivative behavior in the focal region.   To illustrate that the BOR-

FDTD simulator recovers this behavior, in Fig. 6 we compare the time signal along the propagation axis at the focus generated by the 1-cycle pulsed beam with the time derivative of that source signal [Eq. (76)]. The FFT's of these signals are shown in Fig. 7. Only a slight distortion of the signal from the time-derivative behavior is realized. This distortion occurs because the numerical discretization results do not capture all the higher-frequency components in the continuous pulse, as evidenced by the FFT spectra. Higher-resolution grids can mitigate these numerical dispersion effects.

Another plot type was developed to permit us to visualize the focusing effects. An example of this fingerprint plot is shown in Fig. 8. The intensity in the simulation

space is contour plotted as a function of the distance along the axis of propagation and of the time. This results in a spectrogramlike plot of the intensity distribution during the simulation. A horizontal slice yields the intensity as a function of the distance from the aperture for a fixed value of t. A vertical slice yields the intensity as a function of the time t for a fixed distance from the aperture. The location of the focus and the evolution of the derivative behavior of the field are clearly apparent with this visualization approach.

Consider now the designed UWB1 IE pulse introduced in Subsection 4.C. This time signal is compared in Fig. 9 with the 1- and the 10-cycle pulses defined in Subsection 4.D. The 1-cycle pulse has a time record length
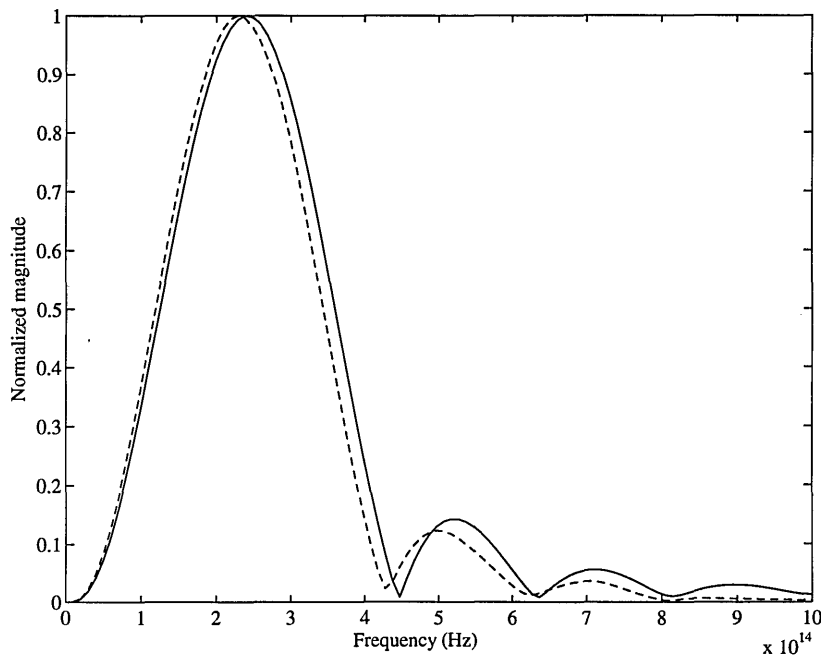

Fig. 7. FFT of the FDTD numerically generated signal at the focus compared with the FFT of the time derivative of the source signal. Solid curves, time derivative of the source signal; dashed curve, FDTD-computed pulse.
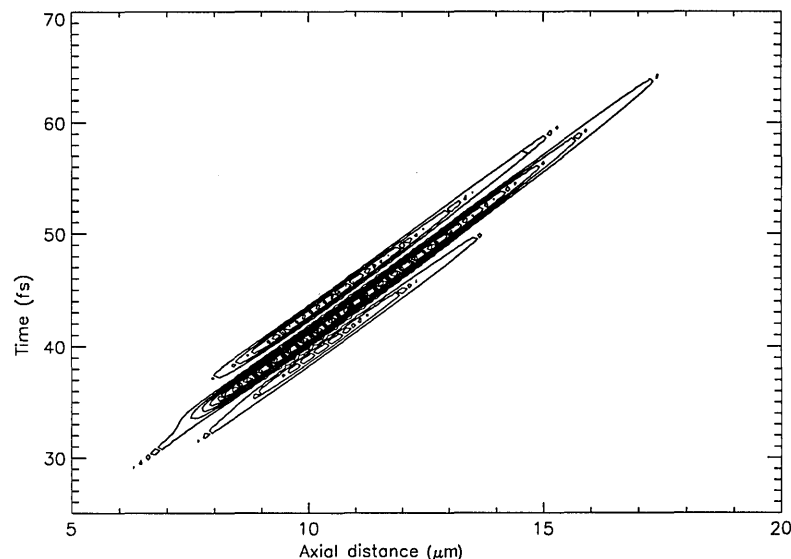

Fig. 8. Intensity in the simulation space contour plotted as a function of the distance along the axis of propagation and of the time. This is a spectrogramlike plot of the field distribution during the simulation. The location of the focus and the evolution of the derivative behavior of the field are clearly apparent with this visualization approach.
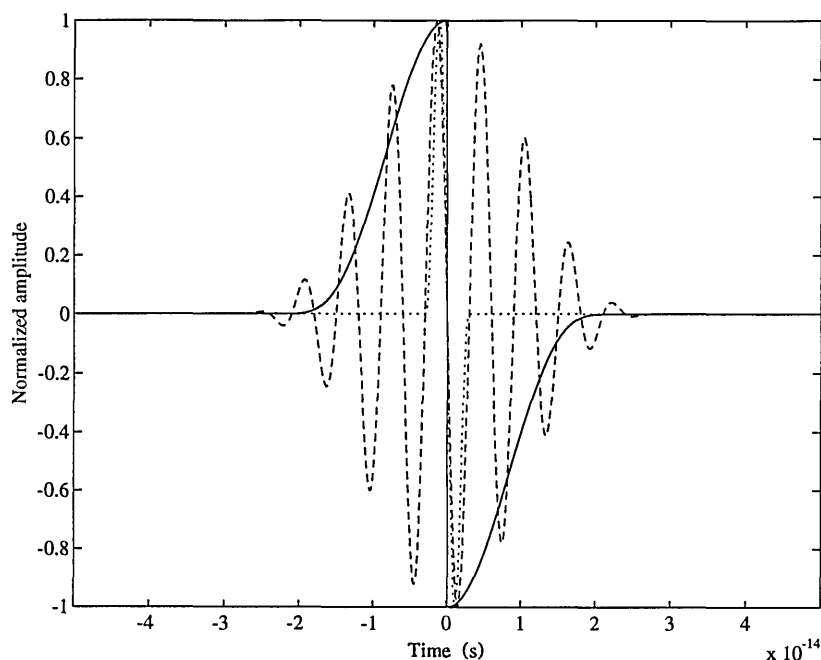
Fig. 9.   10-cycle, 1-cycle, and UWB1 IE pulses plotted as functions of time.   The 1-cycle pulse has a time record length identical to one period of the 10-cycle pulse.   The positive-to-negative switch time is slightly less than one half of one period of the 10-cycle case. Solid curve, UWB1 pulse; dashed curve, 10-cycle pulse; dotted curve, 1-cycle pulse.
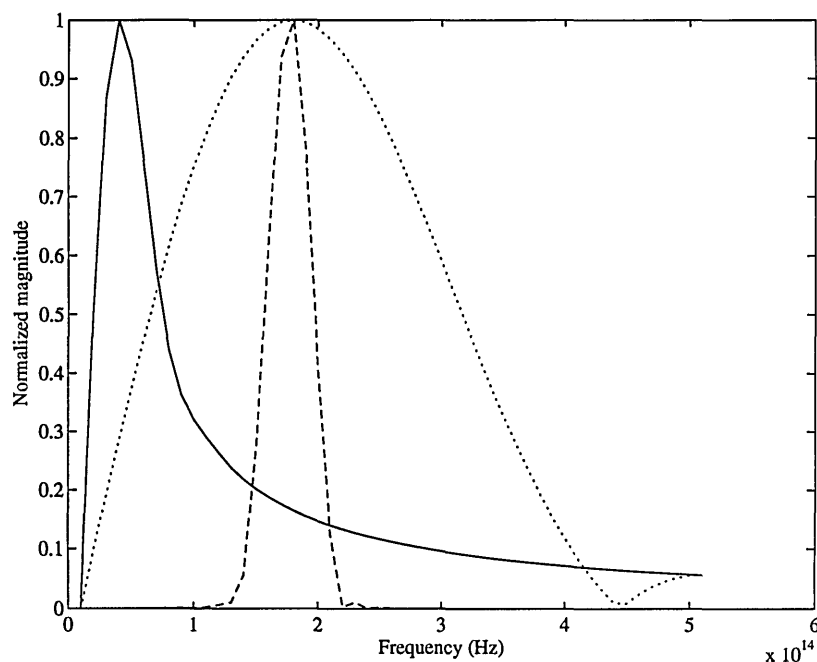

Fig. 10.   FFT's of the 10-cycle, the 1-cycle, and the UWB1 IE pulses plotted as functions of the frequency.   Solid curve, UWB1 pulse; dashed curve, 10-cycle pulse; dotted curve, 1-cycle pulse.

identical to one period of the 10-cycle pulse. The positive-to-negative switch time of the UWB1 IE pulse is slightly less than half of one period of the 10-cycle case. The corresponding magnitudes of the spectra of the 10-cycle, the 1-cycle, and the UWB1 IE pulses are plotted in Fig. 10. One can see that the UWB1 IE pulse has spectral components well above the 1- and the 10-cycle pulses even though there is very little energy initially present in those higher frequencies. Correspondingly, the effective frequencies of these pulses are nearly the same. The maximum intensities along

the propagation axis for the 1-cycle, the 10-cycle, and the UWB1 IE pulses are plotted explicitly in Fig. 11. The corresponding waists are plotted in Fig. 12. We found that the IE is not so high as was predicted, a result partially expected from numerical considerations. The mesh associated with the FDTD approach acts as a low-pass frequency filter; the amount of discretization directly determines the shortest-wavelength components that can be supported by the simulation. The derivative of the UWB1 IE pulse has spectral components that are very high in frequency. It is those short-wavelength

components that are filtered from the simulation that prevented us from reaching the predicted IE factors. We tested this by simulating the much shorter effective-frequency version of the UWB2 IE pulse noted in Subsection 4.D. The simulator reached 70% of the theoretical value for that case with a discretization of $\Delta z = 0.05$ μm. The true UWB1 IE pulse reached an IE value of only 17.8, 13.5% of the theoretical value, with a discretization of $\Delta z = 0.0125$ μm. However, the effective wavelength of the UWB1 pulse is 5.2 times smaller than for the longer-wavelength UWB2 case. We found slightly less than a

doubling of the IE value for each halving of the mesh discretization. Thus we believe that a discretization of $\Delta z = 0.0025$ μm would produce at least a 100-fold IE in the focal region. We do not have the computer resources to test this expectation. Nonetheless the 18-fold value indicates a significant increase in intensity focal strength. Moreover, the filtering effect caused by the numerical simulator in some ways mimics what one might find when dealing with a real source or measurement system that has a finite frequency response. In addition, Fig. 12 shows that the waist of the intensity profile in the
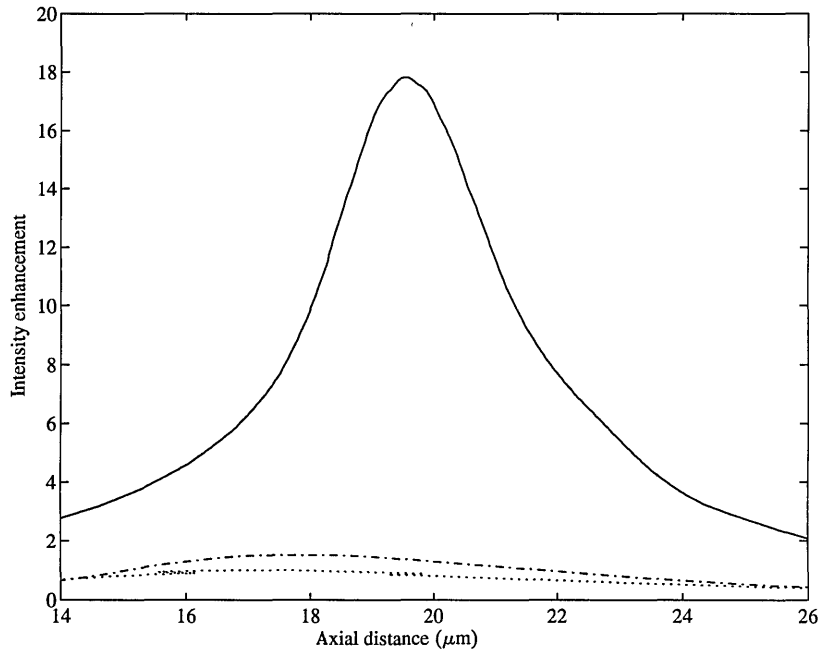

Fig. 11. IE values of the 10-cycle, the 1-cycle, and the UWB1 IE pulsed beams focused by the thin dielectric lens plotted as functions of the distance along the propagation axis. Solid curve, UWB1; dotted–dashed curve, 1-cycle pulse; dotted curve, 10-cycle pulse.
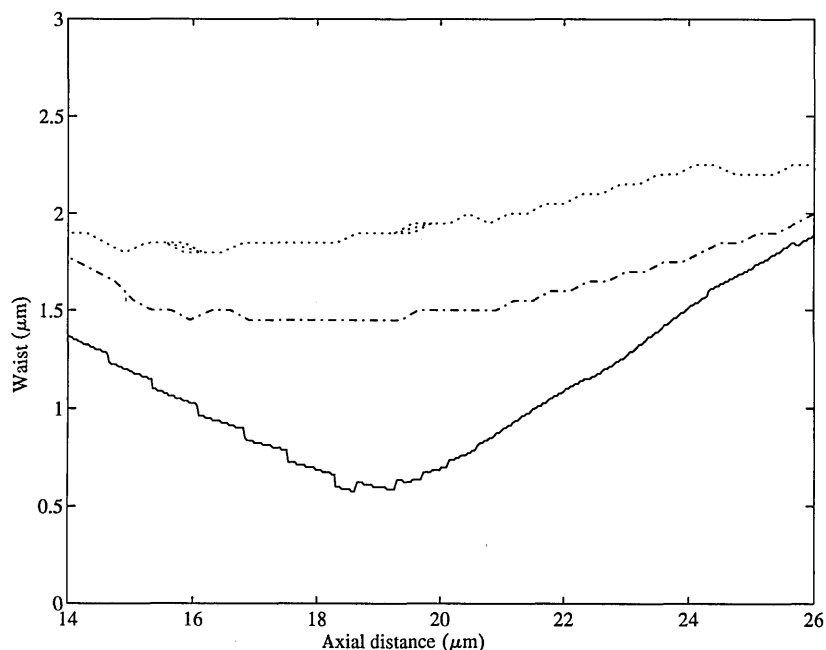

Fig. 12. Waists of the 10-cycle, the 1-cycle, and the UWB1 IE pulsed beams focused by the thin dielectric lens plotted as functions of the distance along the propagation axis. Solid curve, UWB1; dotted–dashed curve, 1-cycle pulse; dotted curve, 10-cycle pulse.
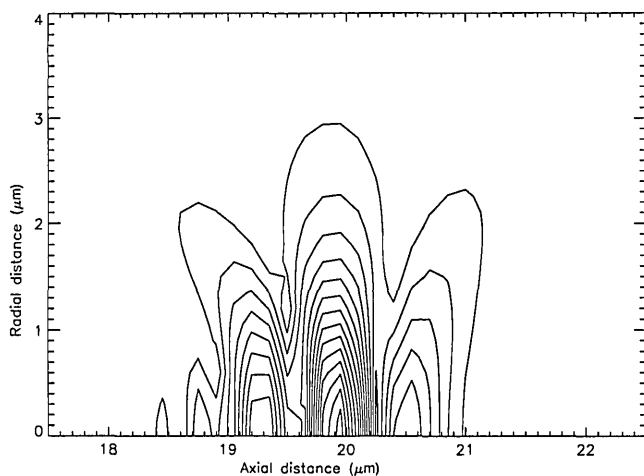
Fig. 13. Contour plot of the E_ρ-field distribution at the time step $n = 750$ in the focal region for the 1-cycle, $F_\# = 1.0$ case. The pulsed beam is at the focus.
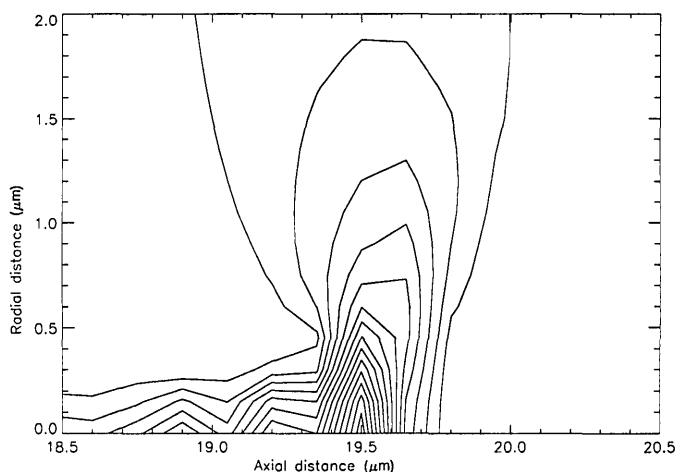

Fig. 14. Contour plot of the E_ρ-field distribution at the time step $n = 3732$ in the focal region for the UWB1 designer pulse, $F_\# = 1.0$ case. The pulsed beam is at the focus.

UWB1 IE pulse, 0.575 μm, is approximately 3.3 times smaller than the 10-cycle value 1.90 μm. This is a very interesting result, since the waist is ~2.5 times smaller than the effective wavelength of the driving signal. It indicates that the intensity focus produced by a well designed UWB pulsed beam can be made sub-effective-wavelength. This means that, by design, we are able to make significant use of the high-frequency components of the pulsed beam even though they contain little energy. In fact, if the predicted intensity value were reached, we would expect the intensity waist to be ~0.21 μm, 6.6 times smaller than the effective wavelength. The spatial-intensity distributions obtained with the simulator in the focal region for the 1-cycle and the UWB1 IE pulse cases are given in Figs. 13 and 14, respectively. Note the slightly different focal lengths that are due to the different effective wavelengths. The time-derivative behavior at the focus of the pulsed beam is clearly present in Fig. 13. In contrast to the 1-cycle case, the significant enhancement of the UWB1 IE pulsed-beam intensity and its narrower intensity waist are apparent in Fig. 14. However, numerical dispersion effects (the pulse's spreading behind the peak near the propagation

axis) in the UWB1 IE case are also discernible. These result from the inadequate resolution of the highest frequencies present in this focused pulsed beam and hinder its expected focal enhancements. It can be seen from Fig. 11 that the focal shift is decreased as the bandwidth of the driving pulses is increased. Thus another advantage of the UWB designer pulse beams is the location of the maximum intensity, which will be nearer the true focus of the lens. This occurs as is expected, since we derive the lens equation [Eq. (79)] by using geometrical optics, a high-frequency approximation to Maxwell's equations.

We extracted the energy and IE results from all the simulations we produced by using the driving-time signals discussed in Subsections 4.C and 4.D. The results for the energy waists and the energy-focusing enhancement factors of the pulsed beams are provided in Table 1. We obtained the numerical energy quantities by computing the intensity everywhere as a function of time and then integrating these intensity time histories. The analytical values are generated with the formulas given in Subsection 4.B. The agreement is quite satisfactory. The corresponding intensity quantities are given in Table 2. Again the agreement between the predicted and the numerical results are generally very satisfactory. However, one striking fact that can be observed from Tables 1 and 2 is the disagreement between the theoretical and the numerical results for the intensity waists. Note, however, that the analytical waists and the focal lengths used in the intensity table are the energy values, since the cw analyses predict that these values are the same. These results clearly demonstrate that the intensity waists are always narrower than the energy waists. As noted above, the nontrivial discrepancies between the simulation and the predicted values for the UWB1 IE pulse can be mitigated, given sufficient computer resources. In summary, for an equivalent input energy these results show that it is possible to design UWB pulsed beams that deliver more intensity to a particular region of space–time than can be delivered by standard cw source signals.

6. CONCLUSIONS

In this paper we have introduced a BOR-FDTD simulation capability that can be applied to rotationally symmetric linear-optics problems. The use of the existing symmetry, for instance, in cylindrical structures leads to an extremely practical approach to modeling three-dimensional problems. In fact, the BOR-FDTD approach allowed us to reduce a computationally intractable, three-dimensional problem to a numerically solvable two-dimensional one. The resulting BOR-FDTD simulator was used to model the propagation of a pulsed Gaussian beam through a thin dielectric lens and the focusing of the resulting pulsed beam.

Analytic results for the lens-focused, pulsed Gaussian beam were also derived. They show that the field in the focal plane is dependent on the time derivative of the initial aperture field. Thus the focal amplification factors are intimately related to the rise time of the driving signals. Moreover, the derived IE factor clearly indicates that, for the same input energy, one can design UWB

Table 1. Comparison of the Focal Lengths, Waist Radii, and Energy-Enhancement Factors Predicted Analytically with the Corresponding Values Obtained from the Energies Computed Numerically by Use of the BOR–FDTD Code[a]

$F_\#$	Source	λ_{rad} (μm)	ω' (μm)		f' (μm)		$\mathcal{FA}_{enrg}$	
			Analytical	FDTD Energy	Analytical	FDTD Energy	Analytical	FDTD
1.0	cw	1.800	1.72	–	16.6	–	9.74	–
1.0	10 cycle	1.796	1.72	1.85	16.6	14.2	9.79	8.71
1.0	3 cycle	1.753	1.67	1.80	16.7	14.5	10.3	9.05
1.0	1 cycle	1.539	1.47	1.60	17.1	14.9	13.3	11.5
1.0	UWB1 (0.05 μm)	1.424	1.36	2.30	17.1	13.9	15.6	3.53
1.0	UWB1 (0.025 μm)			1.52		15.2		5.07
1.0	UWB1 (0.0125 μm)			1.038		16.1		7.01
1.0	UWB2 (0.05 μm)	7.357	7.0	7.0	7.59	7.5	0.577	0.567
1.0	UWB3 (0.05 μm)	1.414	1.35	1.20	17.1	14.3	15.8	9.95
1.0	UWB3 (0.025 μm)			1.075		15.8		11.1
0.707	1 cycle	1.539	0.735	1.05	8.87	7.25	30.4	21.4

[a]Except where noted, $\Delta z = \Delta \rho = 0.05$ μm.

Table 2. Comparison of the Focal Lengths, Waist Radii, and Intensity-Enhancement Factors Predicted Analytically with the Corresponding Values Obtained from the Intensities Computed Numerically by Use of the BOR–FDTD Code[a]

$F_\#$	Source	λ_{rad} (μm)	ω' (μm)		f' (μm)		Y_{int}	
			Analytical	FDTD Intensity	Analytical	FDTD Intensity	Analytical	FDTD
1.0	cw	1.800	1.72	–	16.6	–	1	–
1.0	10 cycle	1.796	1.72	1.80	16.6	14.4	0.996	0.996
1.0	3 cycle	1.753	1.67	1.75	16.7	14.5	0.949	0.950
1.0	1 cycle	1.539	1.47	1.45	17.1	14.5	1.31	1.52
1.0	UWB1 (0.05 μm)	1.424	1.36	1.35	17.1	15.0	132	6.72
1.0	UWB1 (0.025 μm)			0.900		16.1		10.7
1.0	UWB1 (0.0125 μm)			0.575		16.6		17.8
1.0	UWB2 (0.05 μm)	7.357	7.0	2.25	7.59	14.3	24.5	20.52
1.0	UWB3 (0.05 μm)	1.414	1.35	0.825	17.1	15.0	9.87	2.00
1.0	UWB3 (0.025 μm)			0.750		16.0		4.25
0.707	1 cycle	1.539	0.735	1.0	8.87	7.5	1.31	1.45

[a]Except where noted, $\Delta z = \Delta \rho = 0.05$ μm.

driving signals to achieve a significantly larger intensity enhancement than is possible with equivalent cw signals. In addition, the results indicate that the waist of the maximum-intensity profile of a pulsed beam in the focal region can be designed to be much smaller than the waist of the associated energy profile. Several designer pulses were introduced that illustrate how one can achieve these intensity enhancements with UWB signals. These focal region results are related to the far-field behavior of the beams generated by pulse-driven apertures.

The BOR-FDTD simulation results compared very favorably with the analytical predictions. It was demonstrated that the intensity enhancements can be realized with properly designed UWB pulses. Moreover, the numerical results confirmed that there is a substantial difference between a pulsed beam's maximum-intensity behavior and its average energy behavior. These com-

parisons included several different cw and UWB pulses as well as two different lens configurations.

Several issues remain for future investigations. We used only separable space–time beams in a linear system. Further enhancements may be achievable if nonseparable solutions or a nonlinear dielectric lens were used. One might then be able to achieve a true space–time focus and model it accurately with the appropriate BOR-FDTD simulator. Other designer pulses could be developed that may lead to even more favorable results. In particular, we believe that optical experiments could be designed and performed to validate the intensity enhancements reported in this paper. The IE results are scalable to longer-wavelength regimes in which experimental capabilities are already present. For instance, the picosecond-pulse regime is quite accessible now, and many researchers have discussed a variety of pulse-

shaping mechanisms in this regime. Moreover, one can deal with reasonably sized structures at longer wavelengths rather than the micrometer-sized environment modeled here. On the other hand, the numerical BOR-FDTD simulator results that we present demonstrate that the IE effects are achievable in the ultrashort-pulse, ultrasmall-structure regime. Practical applications for these UWB IE systems may include particle acceleration, fiber-optic communications sources and detectors, and photolithography.

APPENDIX A: BODY-OF-REVOLUTION FINITE-DIFFERENCE TIME-DOMAIN EQUATIONS AND BOUNDARY CONDITIONS

The following development is based on Merewether and Fisher,[5] repeated and expanded here for the reasons noted in Subsection 3.A.

Given the Fourier mode decomposition, the equations for each mode are (with the $\partial/\partial\phi$ being evaluated analytically)

$$-\mu\frac{\partial H_{\rho k}}{\partial t} = \left(\frac{-k}{\rho}E_{zk} - \frac{\partial E_{\phi k}}{\partial z}\right), \quad (A1)$$

$$-\mu\frac{\partial H_{\phi k}}{\partial t} = \left(\frac{\partial E_{\rho k}}{\partial z} - \frac{\partial E_{zk}}{\partial \rho}\right), \quad (A2)$$

$$-\mu\frac{\partial H_{zk}}{\partial t} = \frac{1}{\rho}\left[\frac{\partial(\rho E_{\phi k})}{\partial \rho} + kE_{\rho k}\right], \quad (A3)$$

$$\epsilon\frac{\partial E_{\rho k}}{\partial t} + \sigma E_{\rho k} = \left(\frac{k}{\rho}H_{zk} - \frac{\partial H_{\phi k}}{\partial z}\right) - J_{\rho k}, \quad (A4)$$

$$\epsilon\frac{\partial E_{\phi k}}{\partial t} + \sigma E_{\phi k} = \left(\frac{\partial H_{\rho k}}{\partial z} - \frac{\partial H_{zk}}{\partial \rho}\right) - J_{\phi k}, \quad (A5)$$

$$\epsilon\frac{\partial E_{zk}}{\partial t} + \sigma E_{zk} = \frac{1}{\rho}\left[\frac{\partial(\rho H_{\phi k})}{\partial \rho} - kH_{\rho k}\right] - J_{zk}. \quad (A6)$$

Offset grids are set up as in Fig. 15, in the same fashion as the classic Yee algorithm in Cartesian coordinates. The field components are assigned the following locations:

$$H_{\rho k}{}^n(i,j) = H_{\rho k}[\rho_0(i), z(j), t_H(n)], \quad (A7)$$

$$H_{\phi k}{}^n(i,j) = H_{\phi k}[\rho(i), z(j), t_H(n)], \quad (A8)$$

$$H_{zk}{}^n(i,j) = H_{zk}[\rho(i), z_0(j), t_H(n)], \quad (A9)$$

$$E_{\rho k}{}^n(i,j) = E_{\rho k}[\rho(i), z_0(j), t_E(n)], \quad (A10)$$

$$E_{\phi k}{}^n(i,j) = E_{\phi k}[\rho_0(i), z_0(j), t_E(n)], \quad (A11)$$

$$E_{zk}{}^n(i,j) = E_{zk}[\rho_0(i), z(j), t_E(n)]. \quad (A12)$$

J_ρ, J_z, E_ρ, E_z, and H_ϕ are even, and the Fourier expansion is of the form

$$C = C_0 + \sum_{k=1}^{k=k_{max}} C_k \cos(k\phi). \quad (A13)$$

J_ϕ, E_ϕ, H_ρ, and H_z are odd, and the Fourier expansion is of the form

$$D = \sum_{k=1}^{k=k_{max}} D_k \sin(k\phi). \quad (A14)$$

The field components are evaluated in the interleaved grid shown in Fig. 15 at the following positions:

$$\rho_0(i) = (i-1)\Delta\rho + \rho_c, \quad (A15)$$

$$\rho(i) = (i - \tfrac{1}{2})\Delta\rho + \rho_c, \quad (A16)$$

$$z_0(j) = (j-1)\Delta z, \quad (A17)$$

$$z(j) = (j - \tfrac{1}{2})\Delta z, \quad (A18)$$

with $i \in [1, i_{max}]$ and $j \in [1, j_{max}]$, where i_{max} and j_{max} are the number of sample points in ρ and z, respectively, and ρ_c is the radius of the leftmost side of the mesh given in Fig. 15. (The present code uses $\rho_c = 0$; an example of a problem in which a nonzero value would be useful is a coaxial waveguide problem.) The fields are evaluated at the following times:

$$t_H(n) = (n-1)\Delta t, \quad (A19)$$

$$t_E(n) = (n - \tfrac{1}{2})\Delta t, \quad (A20)$$

with $n \in [1, n_{max}]$, where n_{max} is the number of time samples for which the code is run. Using central differencing as in the Yee algorithm, but applying this method now in the cylindrical coordinate system, we may derive the following set of equations for the updates for the **E** and the **H** fields:

$$H_{\rho k}{}^{n+1}(i,j) = H_{\rho k}{}^n(i,j) + \frac{k\Delta t}{\mu\rho_0(i)}E_{zk}{}^n(i,j)$$
$$+ \frac{\Delta t}{\mu}\left[\frac{E_{\phi k}{}^n(i,j+1) - E_{\phi k}{}^n(i,j)}{z_0(j+1) - z_0(j)}\right], \quad (A21)$$

$$H_{\phi k}{}^{n+1}(i,j) = H_{\phi k}{}^n(i,j)$$
$$- \frac{\Delta t}{\mu}\left[\frac{E_{\rho k}{}^n(i,j+1) - E_{\rho k}{}^n(i,j)}{z_0(j+1) - z_0(j)}\right]$$
$$+ \frac{\Delta t}{\mu}\left[\frac{E_{zk}{}^n(i+1,j) - E_{zk}{}^n(i,j)}{\rho_0(i+1) - \rho_0(i)}\right], \quad (A22)$$

$$H_{zk}{}^{n+1}(i,j) = H_{zk}{}^n(i,j)$$
$$- \frac{\Delta t}{\mu}\left\{\frac{\rho_0(i+1)E_{\phi k}{}^n(i+1,j) - \rho_0(i)E_{\phi k}{}^n(i,j)}{\rho(i)\cdot[\rho_0(i+1) - \rho_0(i)]}\right\}$$
$$- \frac{k\Delta t}{\mu\rho(i)}E_{\rho k}{}^n(i,j), \quad (A23)$$

$$B \cdot E_{\rho k}{}^{n+1}(i,j+1) = A \cdot E_{\rho k}{}^n(i,j+1)$$
$$+ \frac{k}{\rho(i)}H_{zk}{}^{n+1}(i,j+1)$$
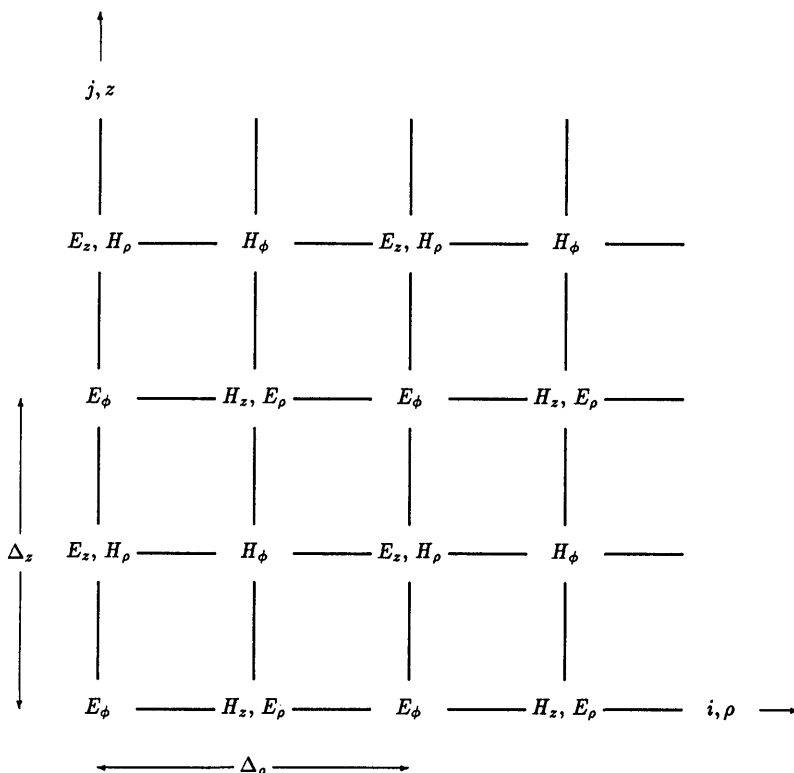$$- \left[\frac{H_{\phi k}{}^{n+1}(i,j+1) - H_{\phi k}{}^{n+1}(i,j)}{z(j+1) - z(j)}\right] - J_{\rho k}, \quad (A24)$$

Fig. 15. Mesh showing interleaved field components.

$$B \cdot E_{\phi k}^{n+1}(i+1, j+1) = A \cdot E_{\phi k}^{n}(i+1, j+1)$$

$$+ \left[\frac{H_{\rho k}^{n+1}(i+1, j+1) - H_{\rho k}^{n+1}(i+1, j)}{z(j+1) - z(j)} \right]$$

$$- \left[\frac{H_{zk}^{n+1}(i+1, j+1) - H_{zk}^{n+1}(i, j+1)}{\rho(i+1) - \rho(i)} \right] - J_{\phi k},$$

$$(A25)$$

$$B \cdot E_{zk}^{n+1}(i+1, j) = A \cdot E_{zk}^{n}(i+1, j)$$

$$+ \left[\frac{\rho(i+1)H_{\phi k}^{n+1}(i+1, j) - \rho(i)H_{\phi k}^{n+1}(i, j)}{\rho_0(i+1) \cdot [\rho(i+1) - \rho(i)]} \right]$$

$$- \frac{k}{\rho_0(i+1)} H_{\rho k}^{n+1}(i+1, j) - J_{zk}, \qquad (A26)$$

with the A, the B, and the $\mathbf{J}$ arrays being defined as

$$A = \left(\frac{\epsilon}{\Delta t} - \frac{\sigma}{2} \right), \qquad (A27)$$

$$B = \left(\frac{\epsilon}{\Delta t} + \frac{\sigma}{2} \right), \qquad (A28)$$

$$J_{\rho k} = J_{\rho k}(t_H^{n+1}), \qquad (A29)$$

$$J_{\phi k} = J_{\phi k}(t_H^{n+1}), \qquad (A30)$$

$$J_{zk} = J_{zk}(t_H^{n+1}), \qquad (A31)$$

all evaluated at the desired E-component location.

For all the above equations except Eq. (A21) (discussed immediately below), $i \in [1, i_{max}]$ and $j \in [1, j_{max}]$, where i_{max} and j_{max} are as previously defined. For the even fields (J_ρ, J_z, E_ρ, E_z, and H_ϕ), $k \in [0, k_{max}]$, where k_{max}

is the number of Fourier modes; for the odd fields (J_ϕ, E_ϕ, H_ρ, and H_z), $k \in [1, k_{max}]$. Equation (A21) has a singularity on the axis ($i = 1$) because of the presence of the term $1/\rho_0(i)$; however, an inspection of Eqs. (A24)–(A26) shows that H_ρ on the axis is never required; hence it may be left out of the computational domain and the index set of i for Eq. (A21) may be relaxed to $i \in [2, i_{max}]$. On the edge of the computational domain the boundary conditions take care of the field behavior, and these values can be computed with Eqs. (A21)–(A26) and can then be overwritten by the field values modified to account for the boundary conditions; this precludes the need for special treatment of the boundary nodes, which is very undesirable, especially in a parallel code.

Note two minor differences between Eqs. (A21)–(A26) and the equations tabulated in Ref. 5, Fig. 10, p. 33: first, there is an error in the signs for E_{zk} in this reference; second, in Eq. (A26), $\rho_0(i)$ has been replaced with $\rho_0(i+1)$. Unless this change is made, the computation for all the points with $i + 1 = 2$ is singular (note that the $\mathbf{E}$ fields are evaluated at $i + 1$), even though these points are off the axis; in Eq. (A26), ρ_0 is now sampled at the same point as the E_z field. Furthermore, some indices that were omitted in Ref. 5, Fig. 10, p. 33 have been added.

We outline the derivation for one of these components, i.e., Eq. (A26). Consider Eq. (A6), repeated here:

$$\epsilon \frac{\partial E_{zk}}{\partial t} + \sigma E_{zk} = \frac{1}{\rho} \left[\frac{\partial(\rho H_{\phi k})}{\partial \rho} - k H_{\rho k} \right] - J_{zk}. \quad (A32)$$

We sample the field in time and space as in Eqs. (A15)–(A20); note that the $\mathbf{E}$ field is sampled in time at a point midway between two $\mathbf{H}$-field samples

and similarly for the spatial samples. Applying central differencing to both the time and the spatial derivatives yields

$$\frac{\partial E_{zk}}{\partial t} \approx \frac{E_{zk}^{n+1}(i,j) - E_{zk}^{n}(i,j)}{\Delta t}, \tag{A33}$$

$$\frac{\partial(\rho H_{\phi k})}{\partial \rho} \approx \frac{\rho(i+1)H_{\phi k}^{n+1}(i+1,j) - \rho(i)H_{\phi k}^{n+1}(i,j)}{\rho_0(i+1) \cdot [\rho(i+1) - \rho(i)]}. \tag{A34}$$

These can now be applied to yield Eq. (A26).

Most of the boundary conditions are obvious: on the top, the bottom, and the right-hand sides of the mesh shown in Fig. 15, the tangential **E** fields must be specified (the ABC described was used for the top and the bottom faces and a perfectly conducting wall for the right-hand face: the grid was large enough for the geometries studied that reflections off this face did not cause problems). However, on axis, the boundary conditions require some explanation.

We derive the boundary condition for E_{z0} by applying the integral form of the Maxwell curl equation in **H** (i.e., Ampere's law),

$$\int_S \nabla \times \mathbf{H} = \oint_C \mathbf{H} \cdot \mathbf{dl} = \int_S \left(\epsilon \frac{\partial \mathbf{E}}{\partial t} + \mathbf{J} + \sigma \mathbf{E} \right) \cdot \mathbf{dS}, \tag{A35}$$

to a small loop of radius r centered at $\rho = 0$ and perpendicular to the z axis. For the case with $k = 0$ one obtains

$$\int_0^{2\pi} H_{\phi 0} \cdot \rho \delta\phi = \int_0^{2\pi} \int_0^{\rho} \left(\epsilon \frac{\partial E_{z0}}{\partial t} + J_{z0} + \sigma E_{z0} \right) \cdot \rho \delta\phi \delta\rho, \tag{A36}$$

which after we approximate E_{z0} as a constant over the surface of the loop yields the following condition for the E_{z0} component on axis:

$$B \cdot E_{z0}^{n+1}(1,j) = A \cdot E_{z0}^{n}(1,j) + \frac{2H_{\phi 0}^{n+1}(1,j)}{\rho(1)} - J_{z0}(1,j)$$
$$\forall j \in [1, j_{max}]. \tag{A37}$$

For the higher-order modes

$$E_{zk}(1,j) = 0 \quad \forall k \in [1, k_{max}] \quad \text{and} \quad j \in [1, j_{max}], \tag{A38}$$

$$E_{\phi k}(1,j) = 0 \quad \forall k \in [1, k_{max}] \quad \text{and} \quad j \in [1, j_{max}]. \tag{A39}$$

ACKNOWLEDGMENTS

REFERENCES

1. R. W. Ziolkowski and J. B. Judkins, "Full-wave vector Maxwell equation modelling of the self-focusing of ultrashort optical pulses in a nonlinear Kerr medium exhibiting a finite response time," J. Opt. Soc. Am. B **10**, 186–198 (1993).
2. K. Yee, "Numerical solution of initial boundary value problems involving Maxwell's equation in isotropic media," IEEE Trans. Antennas Propag. **AP-14**, 302–307 (1966).
3. W. C. Chew, *Waves and Fields in Inhomogeneous Media* (Van Nostrand Reinhold, New York, 1990).
4. A. Taflove and K. R. Umashankar, "The finite-difference time-domain method for numerical modelling of electromagnetics wave interactions with arbitrary structures," in *Finite Element and Finite Difference Methods in Electromagnetic Scattering,* M. A. Morgan, ed., Vol. 2 of Progress in Electromagnetic Research (Elsevier, New York, 1990).
5. D. E. Merewether and R. Fisher, "Finite difference solution of Maxwell's equation for EMP applications," Rep. EMA-79-R-4 (Defense Nuclear Agency, Washington, D.C., 1980).
6. A. C. Cangellaris and R. Lee, "On the accuracy of numerical wave simulations based on finite methods," J. Electromagn. Waves Appl. **6**, 1635–1653 (1992).
7. R. W. Ziolkowski and J. B. Judkins, "Propagation characteristics of ultrawide-bandwidth pulsed Gaussian beams," J. Opt. Soc. Am. A **9**, 2021–2030 (1992).
8. D. B. Davidson, "A parallel processing tutorial," IEEE Antennas Propag. Mag. **32**(4), 6–19 (1990).
9. D. B. Davidson, "Parallel processing revisited: a second tutorial," IEEE Antennas Propag. Mag. **34**(10), 9–21 (1992).
10. R. F. Harrington, *Field Computation by Moment Methods,* 2nd ed. (Krieger, Malabar, Fla., 1982).
11. A. Taflove and K. R. Umashankar, "Advanced numerical modeling of microwave penetration and coupling for complex structures—final report," final Rep. UCRL-15960, Contract 6599805 (Lawrence Livermore National Laboratory, Livermore, Calif., 1987).
12. J. Bailey, "Implementing fine-grained scientific algorithms on the Connection Machine supercomputer," Thinking Machines Tech. Rep. Ser. TR90-1 (Thinking Machines Corporation, Cambridge, Mass., 1990).
13. R. W. Ziolkowski, "Properties of electromagnetic beams generated by ultra-wide bandwidth pulse-driven arrays," IEEE Trans. Antennas Propag. **40**, 888–905 (1992).
14. R. W. Ziolkowski, I. M. Besieris, and A. M. Shaarawi, "Aperture realizations of exact solutions to homogeneous wave equations," J. Opt. Soc. Am. A **10**, 75–87 (1993).
15. G. C. Sherman, "Short pulses in the focal region," J. Opt. Soc. Am. A **6**, 1382–1387 (1989).
16. Z. Bor and Z. L. Horváth, "Distortion of femtosecond laser pulse in lenses. Wave optical description," Opt. Commun. **94**, 249–258 (1992).
17. J. J. Stamnes, *Waves in Focal Regions* (Hilger, London, 1986).
18. A. Yariv, *Quantum Electronics,* 2nd ed. (Wiley, New York, 1975).
19. I. S. Gradshteyn and I. M. Ryzhik, eds., *Tables of Integrals, Series and Products* (Academic, New York, 1965).